



UNIVERSITY OF LEEDS

This is a repository copy of *The role of antecedent morphology and changing sediment sources in the postglacial palaeogeographical evolution of an incised valley: The sedimentary record of the Ría de Arousa (NW Iberia)*.

White Rose Research Online URL for this paper:

<https://eprints.whiterose.ac.uk/182382/>

Version: Accepted Version

---

**Article:**

Cartelle, V, García-Moreiras, I, Martínez-Carreño, N et al. (2 more authors) (2022) The role of antecedent morphology and changing sediment sources in the postglacial palaeogeographical evolution of an incised valley: The sedimentary record of the Ría de Arousa (NW Iberia). *Global and Planetary Change*, 208. 103727. ISSN 0921-8181

<https://doi.org/10.1016/j.gloplacha.2021.103727>

---

© 2021, Elsevier. This manuscript version is made available under the CC-BY-NC-ND 4.0 license <http://creativecommons.org/licenses/by-nc-nd/4.0/>.

**Reuse**

This article is distributed under the terms of the Creative Commons Attribution-NonCommercial-NoDerivs (CC BY-NC-ND) licence. This licence only allows you to download this work and share it with others as long as you credit the authors, but you can't change the article in any way or use it commercially. More information and the full terms of the licence here: <https://creativecommons.org/licenses/>

**Takedown**

If you consider content in White Rose Research Online to be in breach of UK law, please notify us by emailing [eprints@whiterose.ac.uk](mailto:eprints@whiterose.ac.uk) including the URL of the record and the reason for the withdrawal request.



[eprints@whiterose.ac.uk](mailto:eprints@whiterose.ac.uk)  
<https://eprints.whiterose.ac.uk/>

1        **The role of antecedent morphology and changing sediment sources in the postglacial**  
2        **palaeogeographical evolution of an incised valley: the sedimentary record of the Ría de**  
3        **Arousa (NW Iberia)**

4        Víctor Cartelle\*<sup>1,2,3</sup>, Iría García-Moreiras<sup>2,4</sup>, Natalia Martínez-Carreño<sup>2,3</sup>, Castor Muñoz  
5        Sobrino<sup>2,4</sup>, Soledad García-Gil<sup>2,3</sup>

6        <sup>1</sup>School of Earth and Environment, University of Leeds, UK; <sup>2</sup> Centro de Investigación Mariña,  
7        Universidad de Vigo, Spain; <sup>3</sup>Dept. Xeociencias Mariñas, Universidade de Vigo, Spain; <sup>4</sup>Dept.  
8        Bioloxía Vexetal e Ciencias do Solo, Universidade de Vigo, Spain

9        \*Corresponding author: Víctor Cartelle: v.cartellealvarez@leeds.ac.uk

10       **Abstract**

11       Incised valleys represent dynamic coastal and shelf systems in continuous change in response  
12       to different temporal and spatial scales. Their sedimentary record offers valuable data to  
13       unveil the effect of different drivers, such as relative sea-level rise, on the evolution of coastal  
14       systems and provide invaluable records of palaeoenvironmental changes. In this work, the  
15       palaeogeographical evolution of the Ría de Arousa (NW Spain) from the Last Glacial Maximum  
16       to the present is reconstructed by identifying the main elements of sedimentary architecture.  
17       These elements are characterised using a multidisciplinary approach combining seismic,  
18       sedimentary, geochemical and palynological data. The general succession of the sedimentary  
19       infilling of the incised valley records an overall transgression in response to postglacial sea-  
20       level rise. A large fluvial valley evolves into a tide-dominated estuary and later to a wave-  
21       dominated estuary as it is progressively flooded. The complex interaction between variable  
22       rates of relative sea-level rise and the antecedent morphology exerts a strong control on  
23       hydrodynamics within the valley controlling the sediment dynamics and facies distribution,  
24       displaying some similarities with conceptual facies models for tide- and wave-dominated  
25       estuaries. The analysis of sediment sources also denotes significant changes in response to

26 varying hydrodynamic regimes and climate, shifting from a predominant fluvial source in the  
27 earliest phases of the transgression to an increase in local sources (cliffs and local coastal  
28 deposits), including a likely reworking of older deposits (sediment recycling) during the Early  
29 Holocene. These changing sediment sources may have a clear impact on the palynological  
30 signal recorded within the incised valley, hypothetically masking and overprinting the climatic  
31 signal during phases of intense reworking of older deposits. Sediment recycling seems  
32 extensive within the incised valley and represents a key process that needs to be evaluated to  
33 understand the source-to-sink sediment flux to the deeper ocean. Its impact on the  
34 sedimentary records may have major implications for palaeoenvironmental studies in coastal  
35 settings, stressing the importance of applying multi-proxy approaches.

36 **Keywords:** incised valley, sea level, tide-dominated estuary, wave-dominated estuary,  
37 sedimentary environments, sedimentary facies, seismic facies, sediment recycling

38

39 **1. Introduction**

40 Incised valleys are elongated palaeotopographic lows commonly found on continental  
41 shelves and coastal plains developed by fluvial erosion in response to relative sea-level fall,  
42 subsequently flooded and infilled by fluvial, coastal and marine processes during relative sea-  
43 level rise. Their fill typically reflects this succession of processes, featuring basal fluvial  
44 sediments which are overlaid by estuarine and marine deposits (Allen and Posamentier, 1994;  
45 Ashley and Sheridan, 1994; Blum et al., 2013; Boyd et al., 2006; Dalrymple et al., 1994; Wang  
46 et al., 2020; Zaitlin et al., 1994). The sedimentary fill of incised valleys records the complex  
47 interplay of varied controlling factors, including sea-level fluctuations, climate, tectonics and  
48 sediment supply, and therefore reveal valuable information about earth-surface processes and  
49 the depositional history (Chaumillon et al., 2010; De Santis and Caldara, 2014; Mattheus and  
50 Rodriguez, 2011; Wang et al., 2020, 2019). In addition to these drivers, the role of antecedent  
51 morphology (either determined by the bedrock or by the pre-existent deposits) has recently  
52 gained more attention as a key factor explaining not only the complicated architecture  
53 recorded within incised valleys (Cartelle and García-Gil, 2019; Chaumillon et al., 2010, 2008;  
54 Gomes et al., 2016; Green, 2009; Menier et al., 2006; Ximenes Neto et al., 2021) but also  
55 exerting a strong control on the evolution of various coastal systems and shelf settings (e.g.  
56 Belknap and Kraft, 1985; Bortolin et al., 2019; Emery et al., 2019; Engelbrecht et al., 2020;  
57 Kirkpatrick and Green, 2018; Rangel and Dominguez, 2020; Rodriguez et al., 2005).

58 Incised-valley systems, coastal and shelf areas play critical roles in transferring  
59 sediments from hinterland regions to deep-marine environments and constitute an essential  
60 segment of the source-to-sink framework, being subject to the complex dynamics of the  
61 shoreline (Allen, 2017; Sømme et al., 2009). A wide range of marine processes act in this  
62 segment, modifying the sediment routes and storage, and ultimately determining the amount  
63 of sediment delivered to more distal environments (Allen, 2017, 2008; Sømme et al., 2009). It

64 is vital to understand the role of hydrodynamic processes in these areas and their interaction  
65 with allogenic drivers such as climate and sea-level fluctuations to determine the fate of  
66 sediments in these “transfer areas”, as well as the time and spatial scales at which they  
67 operate (Voller et al., 2020). Additionally, environmental signals are propagated through these  
68 segments and their boundaries at a range of time and space scale (Romans et al., 2016), but  
69 they also change and are masked, buffered or even shredded (Jerolmack and Paola, 2010;  
70 Straub et al., 2020; Toby et al., 2019), leaving an incomplete record that is later used to  
71 reconstruct past changes. Understanding the incompleteness or imperfection of these archives  
72 is also critical to perform better informed palaeoenvironmental reconstructions (Straub et al.,  
73 2020).

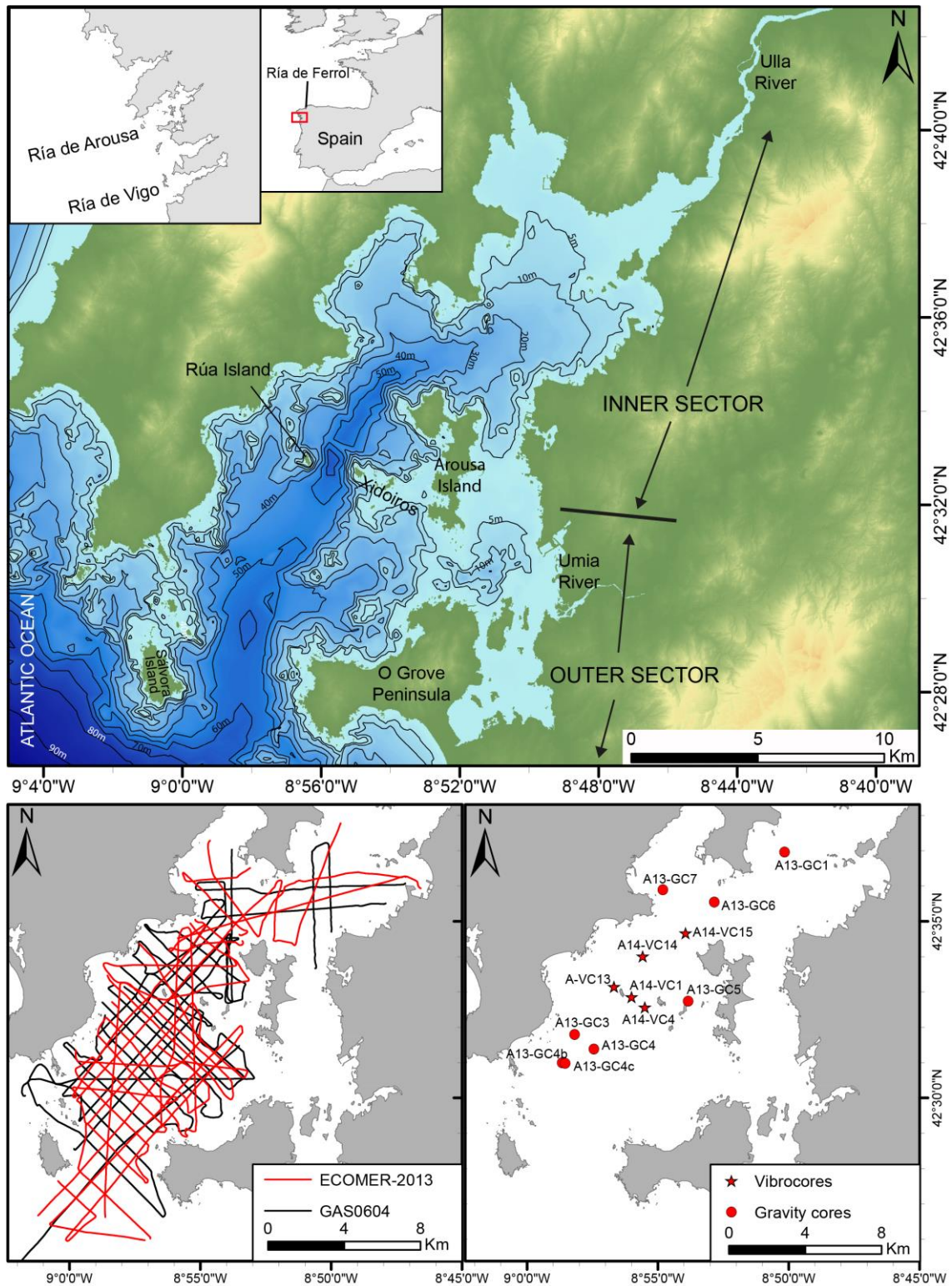
74         The coast of Galicia (north-west Iberia) features several incised valleys, called rias,  
75 distributed along 1720 km of coast with a long history of research (e.g. Cartelle and García-Gil,  
76 2019; Cotton, 1956; García-García et al., 2005; García-Gil et al., 1999; García-Moreiras et al.,  
77 2019a, 2019b; Martínez-Carreño and García-Gil, 2017; Muñoz-Sobrino et al., 2012; Nonn,  
78 1966; Rey, 1993; Rey and Somoza, 1993). These valleys were generated by tectonic modeling  
79 of the rocky basement during the Tertiary, and erosion and infill during the subsequent sea-  
80 level fluctuations associated with Quaternary glacial/interglacial cycles (Cotton, 1956; García-  
81 Gil et al., 1999; Martínez-Carreño and García-Gil, 2017; Pannekoek, 1970; Torre Enciso, 1958).  
82 The Ría de Arousa [RdA] is the largest and deepest among all these incised valleys and  
83 represents the most complete submerged record of palaeoenvironmental changes in the  
84 region since the Last Glacial Maximum [LGM] (García-Moreiras et al., 2019a). The stratigraphy  
85 of the RdA valley was previously studied by applying only seismic reflection techniques, and  
86 most of the deposits found within the incised valley were interpreted to correspond to the last  
87 glacial cycle (e.g. Diez, 2006; Hinz, 1970; Rey, 1993; Rey and Somoza, 1993). The first study  
88 integrating sediment sampling and geophysical data was carried out by García-Moreiras et al.  
89 (2019a) and focused on analysing palaeoenvironmental changes occurring during the Late

90 Glacial to Early Holocene transition by means of palynological analyses performed on a  
91 sediment core. In the present work, seismic and sedimentary facies are combined with  
92 radiocarbon age control and geochemical proxies to reconstruct the history and depositional  
93 environments in the Ría de Arousa incised valley during the postglacial. The main objectives  
94 are to describe and analyse the elements of the depositional architecture preserved in the  
95 sedimentary fill, reconstruct palaeogeographical changes and investigate the role of  
96 antecedent morphology and changing hydrodynamics on incised valley evolution.

## 97 **2. Study area**

98         The Ría de Arousa (Fig. 1) is the largest of all the Galician rias, with a surface area of  
99 230 km<sup>2</sup> and a volume of 4.5 x 10<sup>9</sup> m<sup>3</sup>. The basin is characterised by a complex physiography,  
100 displaying an irregular coastline with numerous smaller bays in the northern margin and  
101 several islands (the largest one being the Arousa Island, Fig. 1) and a large peninsula in the  
102 southern margin (O Grove Peninsula, Fig. 1). The RdA has two connections with the shelf. The  
103 main connection is located between the Sálvora Island and the O Grove Peninsula; it is called  
104 the southern mouth and is characterised by a maximum depth of 70 m and a width of 4.8 km.  
105 The second connection, the northern mouth, has a maximum depth of 10 m and is located to  
106 the north of Sálvora Island, being 3.5 km wide. This mouth has several small islands distributed  
107 between Sálvora and the northern coast. The central axis of the RdA is ENE-WSW-oriented in  
108 the inner sector, NE-SW towards the outer sector and almost N-S near its mouth. The  
109 boundary between the outer and inner sectors is determined by the location of a submerged  
110 strait between the Rúa Island and the Xidoiros Islands (Fig. 1). The length along the axis is 30  
111 km, with a variable width that reaches a maximum of 14 km. A secondary basin can be  
112 recognised in the SW of the ria, at the back of the Arousa Island (Fig. 1), with an N-S  
113 orientation and a maximum depth of 20 m, although its depth is generally lower than 10 m.

114 The Galician margin is characterised by a narrow continental shelf (ca. 30 km) with the shelf  
 115 break at -150 m below present sea level (Fernández-Salas et al., 2015).



116

117 **Figure 1. Location of the study area, showing seismic track lines and vibro/gravity core positioning.**

118

119

120           The Atlantic coast of Galicia is a mesotidal coast with a mean tidal range of 3 m and a  
121 semi-diurnal cycle and is located at the northern margin of the NW African coastal upwelling  
122 system. The RdA is characterised by a two-layered positive residual circulation which is  
123 modified by upwelling/downwelling events, determined by the wind pattern (Fraga, 1981;  
124 Rosón et al., 1997, 1995; Wooster et al., 1976). The most relevant fluvial contributions to the  
125 RdA are those from the Ulla and Umia rivers (Fig. 1). The Ulla river flows into the innermost  
126 part of the ria and drains a catchment area with a total extension of 2803 km<sup>2</sup>. This is a  
127 dendritic basin with high permeability and low surface runoff. The mean annual discharge of  
128 the Ulla river, estimated at its mouth, is 79.3 m<sup>3</sup>/s (Río Barja and Rodríguez Lestegás, 1992).  
129 The Umia river flows into the east of the ria, draining 440 km<sup>2</sup>, with a mean annual discharge  
130 estimated at its mouth of 16.4 m<sup>3</sup>/s (Río Barja and Rodríguez Lestegás, 1992).

### 131 **3. Methodology**

132           The data analysed here were acquired on board the R/V Mytilus during three surveys  
133 from 2004 to 2015: GAS0604, ECOMER13 and ECOMER14-2. Eight gravity cores and five vibro-  
134 cores were recovered from selected sites, together with more than 1100 km of high-resolution  
135 seismic records (Fig.1).

136           The gravity and vibro-corer consisted of a 4-m-long, 9-cm-diameter steel core barrel.  
137 The gravity-corer was ballasted at the top with more than 500 kg of lead, while the vibro-corer  
138 had a vibration and water-pumping system. Sediment cores were split lengthwise, described  
139 and sampled for analysis in the CACTI laboratory of the University of Vigo. Particle-size  
140 distribution was analysed by laser diffraction using a Beckman Coulter LS 13 320, and the  
141 results were classified following Wentworth's (1992) nomenclature. Total organic carbon [TOC]  
142 and total inorganic carbon [TIC] were determined for samples taken at regular intervals using a  
143 LECO CNS2000. An ITRAX core scanner has also been used to perform X-Ray Fluorescence



144 [XRF] elemental analyses of the cores. Several proxies derived from XRF-data are integrated  
145 into the sedimentary facies analyses. Si, Ti and Fe were selected as proxies indicative of  
146 terrigenous sediment delivery (Blanchet et al., 2007; Haug et al., 2003, Kleiven et al., 2007,  
147 Rothwell and Croudace, 2015), with Ti/Ca ratio showing the relative contribution of lithogenic  
148 and biogenic sediments (Tjallingii et al., 2010). Zr/Rb ratio provides a grain-size proxy, with  
149 higher values indicative of a higher content in coarse particles (Wang et al., 2011). K/Ti ratio  
150 denotes provenance differences of detrital material (Arribas et al., 2010, Cartelle and García-  
151 Gil, 2019, Diekmann et al., 2008). Well-preserved articulated valves without signatures of  
152 reworking were selected for radiocarbon dating (Table 1), performed at Beta Analytic  
153 Laboratory (USA). All radiocarbon dates are given in calibrated years before present (cal a BP)  
154 after calibration using Calib Rev 8.20 (Stuiver et al., 2021). For bivalve shells, the Marine20  
155 radiocarbon calibration curve (Heaton et al., 2020) has been used, with a local reservoir  
156 correction of  $12 \pm 163$  (Soares and Dias, 2007). Sediment core A14-VC15 was also subject to  
157 palynological analyses by García-Moreiras et al. (2019a).

158         Seismic data was acquired using a towed boomer source (Applied Acoustics AA200)  
159 and a single-channel streamer (Applied Acoustics AAE 8), recording location using a differential  
160 global positioning system (Trimble AgGPS 132, error <1 m). Interpretation of seismic facies and  
161 units was conducted according to the basic principles of seismic stratigraphy (Mitchum, 1977,  
162 Mitchum and Vail, 1977, Mitchum et al., 1977). Seismic facies were characterised following  
163 Mitchum et a. (1977) and were used to define seismic stratigraphic units. Key horizons were  
164 mapped, interpreted and gridded to maps using the flex gridding algorithm in Kingdom (IHS  
165 Markit). Time-to-depth conversion to tie cores and seismic data has been done assuming a  
166 sound velocity of 1600 m/s for unconsolidated sediments (Hamilton, 1980; Hamilton and  
167 Bachman, 1982).

#### 168 **4. Results**

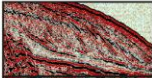
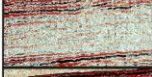


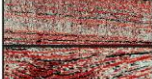


169 **4.1 Seismic units**

170           The analysis of the RdA seismic records has allowed the recognition of seven seismic  
171 facies (Fig. 2) that allows the identification of up to nine seismic units within the sedimentary  
172 fill of the incised valley. The present study focuses on the four youngest seismic units (U6 to  
173 U9, Fig. 3) corresponding to the postglacial record following interpretations by García-Moreiras  
174 et al. (2019a). For simplicity, the same terminology for seismic units used in previous studies is  
175 maintained here.

176 Table 1. Table summarizing radiocarbon dates used in this study, their calibration and their correspondence with seismic units.

Core	Average core depth (cm)	Laboratory Ref.	Material dated	Conventional radiocarbon age	d13C	d18O	Calibrated age (cal a BP)*	Seismic unit
<b>A13-GC3</b>	320.5	Beta-494797	Bivalve shell	3450±30 BP	0.8	2.5	2730-3545	U9 <sup>178</sup>
<b>A13-GC4</b>	179	Beta-494795	Bivalve shell	3350±30 BP	-1.8	1.7	2615-3440	U9
<b>A13-GC4</b>	236.5	Beta-494796	Bivalve shell	8630±30 BP	1.3	0.9	8600-9460	U9
<b>A13-GC7</b>	112.5	Beta-415353	Bivalve shell	3190±30 BP	1.6		2370-3240	U9
<b>A14-VC4</b>	46.5	Beta-415343	Bivalve shell	3970±30 BP	1.7		3350-4240	U9
<b>A14-VC4</b>	140.5	Beta-415344	Bivalve shell	11980±40 BP	2.0		12920-13700**	U7
<b>A14-VC4</b>	155	Beta-401170	Bivalve shell	11930±40 BP	1.1		12850-13620**	U7
<b>A14-VC4</b>	181.5	Beta-415345	Bivalve shell	11930±40 BP	1.2		12850-13620**	U6
<b>A14-VC4</b>	274	Beta-401171	Bivalve shell	12230±40 BP	0.1		13180-14000	U6
<b>A14-VC13</b>	30.5	Beta-415350	Bivalve shell	2420±30 BP	1.5		1465-2305	U9
<b>A14-VC13</b>	86.5	Beta-415351	Bivalve shell	3750±30 BP	1.3		3065-3955	U9
<b>A14-VC13</b>	158	Beta-415352	Bivalve shell	5770±30 BP	1.0		5580-6325	U8
<b>A14-VC13</b>	242.5	Beta-401172	Bivalve shell	6560±30 BP	-0.2		6435-7225	U8
<b>A14-VC14</b>	66	Beta-415348	Bivalve shell	1570±30 BP	1.6		625-1295	U9
<b>A14-VC14</b>	174.5	Beta-415349	Bivalve shell	8160±30 BP	1.3		8080-8940	U7
<b>A14-VC14</b>	202	Beta-401173	Bivalve shell	9170±30 BP	0.3		9330-10180	U7
<b>A14-VC15</b>	31	Beta-415346	Bivalve shell	4670±30 BP	1.0		4235-5170	U9
<b>A14-VC15</b>	49.5	Beta-411507	Bivalve shell	8740±40 BP	-1.8		8700-9590	U9
<b>A14-VC15</b>	81.5	Beta-411508	Bivalve shell	9140±30 BP	1.5		9290-10170	U7
<b>A14-VC15</b>	108.5	Beta-401174	Bivalve shell	9890±30 BP	0.8		10190-11120**	U7
<b>A14-VC15</b>	121.5	Beta-415347	Bivalve shell	9590±30 BP	1.3		9760-10780	U7
<b>A14-VC15</b>	154	Beta-411509	Bivalve shell	9770±40 BP	1.2		10110-11070	U6
<b>A14-VC15</b>	277.5	Beta-401175	Bivalve shell	12510±40 BP	-0.4		13450-14500	U6

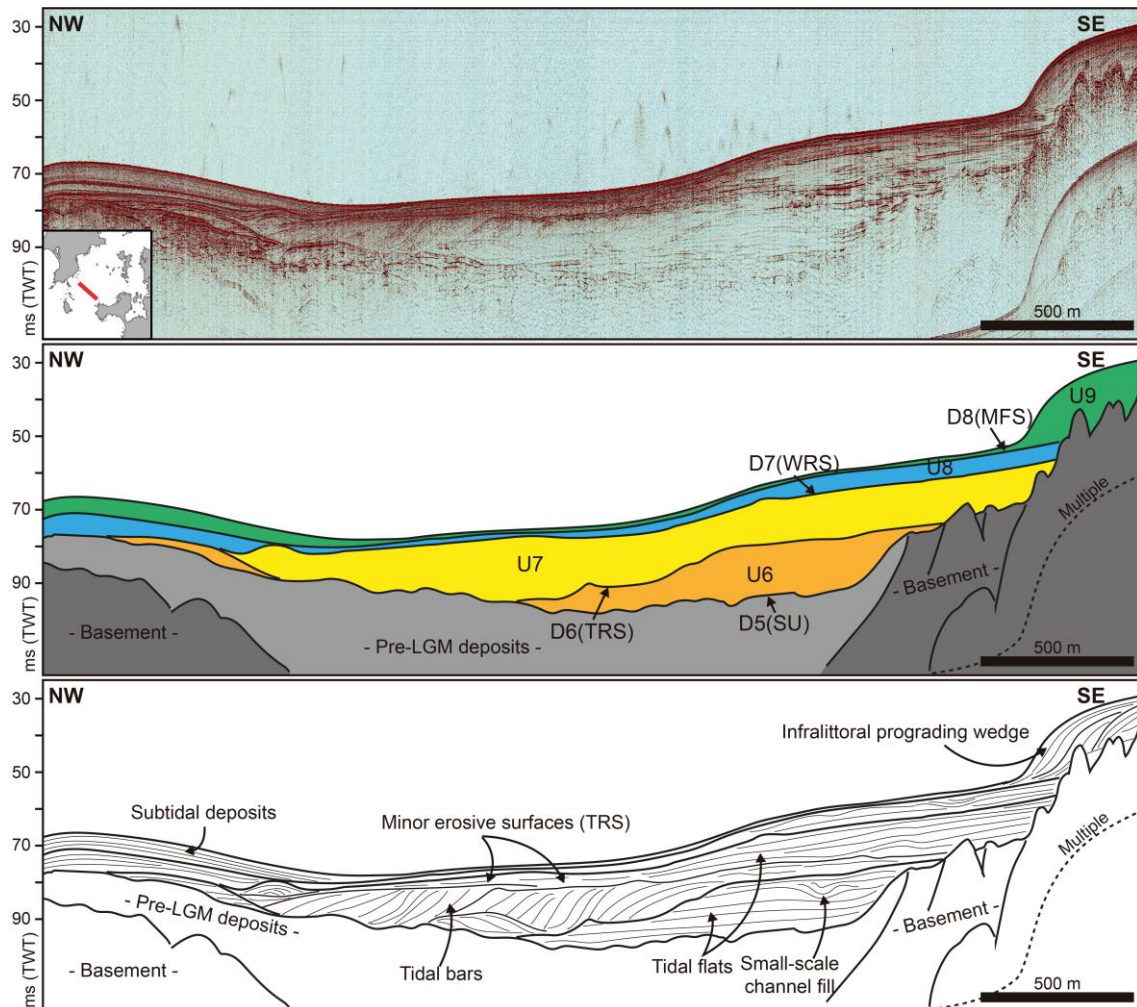
\*Rounded to the nearest 5 (<10000) or 10 (>10000) \*\*Discarded ages, probably reworked material

Facies	Illustration	Seismic facies			Reflector Configuration	Outer shape or geometry	Interpretation [Units]
		Frequency	Amplitude	Continuity			
sf6		Medium	High to medium	High	Prograding (sigmoid and oblique)	Lens Fan Wedge	Tidal sand bars [U6/U7] Storm fans [U8/U9] Infralitt. prog. wedges [U9]
sf5		Medium	Medium	High to medium	Subparallel aggrading	Sheet	Tidal flats [U6/U7]
sf4		-	High	Very low	Prograding Almost chaotic	Wedge	Bayhead delta [U6 ]
sf3		High	High	High	Parallel aggrading	Sheet Lens	Subtidal deposits [U8/U9]
sf2		High	Medium	High to medium	Parallel aggrading	Sheet Sheet drape Channel fill	Subtidal deposits [U8/U9] Tidal flats [U6/U7/U8/U9] Channel fills [U6/U7] Tidal inlet [U7/U8]
sf1		Medium	High	Medium	Subparallel aggrading	Channel fill	Channel fills [U6/U7] Tidal inlet [U7/U8]
sfG		-	-	-	Chaotic	Acoustic turbidity	Gas in the sediments [U8/U9]

179

180 **Figure 2. Description of the seismic facies identified on the seismic profiles. Outer shape terminology**  
 181 **is based on Mitchum et al. (1977). The interpretation is based on sedimentary facies and facies**  
 182 **associations (see text for details).**

183 Seismic unit U6 rests on the basal disconformity D5, which mainly corresponds to an  
 184 onlap surface, while disconformity D6 represents its top and truncates the internal reflectors  
 185 of the unit (Fig. 3). Disconformity D6 is erosive in the axis of the ria, where it even reworks  
 186 disconformity D5 (Fig. 3). This unit is mainly located along the axis of the ria and in areas where  
 187 the erosion of disconformity D5 was deeper, resting above older units. The highest  
 188 thicknesses, up to 22 ms TWT (17.6 m), are reached in the inner sector of the ria. Four  
 189 radiocarbon dates have been obtained from sediments of this unit (Table 1, Fig. 4), with ages  
 190 between 13450-14500 cal a BP and 10110-11070 cal a BP, so this unit mainly corresponds to  
 191 the Upper Pleistocene-Holocene transition.



192

193 **Figure 3. Representative seismic profile and interpretation panel in the Ría de Arousa incised valley**  
 194 **showing the main seismic stratigraphic units and surfaces, and elements of sedimentary architecture.**  
 195 **LGM: Last Glacial Maximum; SU: Subaerial Unconformity; TRS: Tidal Ravinement Surface; WRS: Wave**  
 196 **Ravinement Surface; MFS: Maximum Flooding Surface; ms TWT: milliseconds two-way travel time.**

197        Seismic unit U7 is bounded at its base by disconformity D6, which represents both an  
 198 onlap and a downlap surface (Fig. 3), while its top corresponds to disconformity D7, a smooth  
 199 and subhorizontal erosive truncation, with a greater erosive character towards the margins of  
 200 the ria (Fig. 3). This unit occupies a slightly larger extension than the underlying U6, occurring  
 201 mainly on the axis of the ria overlying U6 or above older units. U7 reaches its greatest  
 202 thickness in the centre of the study area (up to 21 ms TWT - 16.8 m), where large-scale  
 203 channel fills occur. Towards the outer sector, a complex of channels and prograding bodies (as  
 204 shown in Fig. 3) and several locally relevant erosive surfaces are identified, indicating different  
 205 phases of sedimentation/erosion throughout the evolution of these complexes. However,

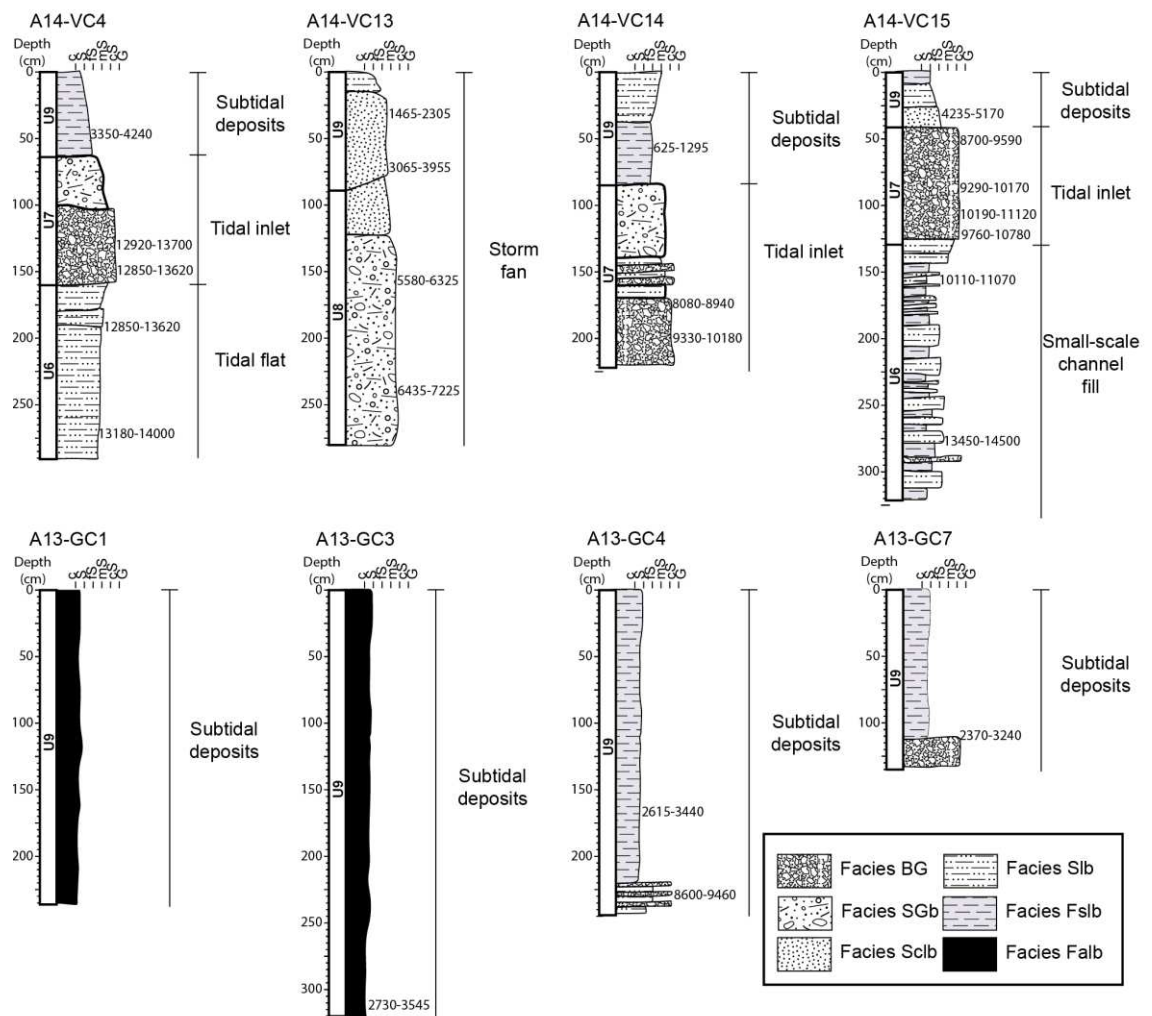
206 these surfaces are of local occurrence and cannot be traced across the entire incised valley.  
207 From the recovered sedimentary material, up to eight radiocarbon dates have been obtained  
208 (Table 1, Fig. 4) with age ranges between 12850-113620 cal a BP and 8080-8940 cal a BP.  
209 Although whole bivalve shells have been used, with both valves whenever possible and  
210 without clear signs of reworking, some of the ages obtained are clearly of reworked material  
211 and have been discarded (Table 1).

212 Seismic unit U8 is deposited above disconformity D7, which fundamentally constitutes  
213 an onlap surface (Fig. 3), although locally downlap terminations are differentiated. The top of  
214 the unit corresponds to disconformity D8, which is apparently conformable, but locally erosive  
215 truncation is also identified. U8 is more expansive and appears in most of the incised valley  
216 resting on U7 or older units. It is a thin unit that generally does not exceeds 6 ms TWT (4.8 m)  
217 of thickness, although locally, it reaches up to 11 ms TWT (8.1 m). The radiocarbon data  
218 obtained spans ages between 6435-7225 and 5580-6325 cal a BP (Table 1, Fig. 4), although  
219 these are not from either the base or the top of the unit. Considering the chronological  
220 framework of the other units, U8 is attributed to an approximate age range between 8 and 5  
221 cal ka BP.

222 Seismic unit U9 is the most recent unit in the sedimentary fill of the RdA, bounded at  
223 its base by discontinuity D8, which represents a downlap surface towards the basin margins,  
224 being conformable in the axis of the ria (Fig. 3). Its top coincides with the present seafloor. The  
225 higher thicknesses of this unit (up to 30 ms TWT - 24 m) are located towards the margins of the  
226 RdA, coinciding with the presence of large-scale prograding sedimentary bodies that generally  
227 migrate towards the axis of the valley where the thickness of this unit is lower (Fig. 3). U9 is  
228 expansive and is deposited above U8 or directly overlying the rocky basement. The  
229 radiocarbon ages obtained (Table 1, Fig. 4) vary from 4235-5170 to 625-1295 cal a BP.

#### 230 **4.2. Sedimentary facies and proxies**





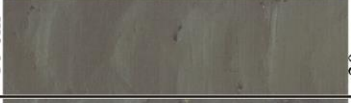

231 A total of six sedimentary facies were identified in the sediment cores and are  
 232 summarised in figures 4 and 5. Several proxies (including TOC, TIC, Si, Fe, and Zr/Rb, Ti/Ca and  
 233 K/Ti ratios) were also analysed on selected cores (Fig. 6). Analysis of facies and facies  
 234 associations (both seismic and sedimentary, Figs. 2 and 5) was used to identify larger-scale  
 235 elements of the sedimentary architecture to recognise sedimentation of various depositional  
 236 environments within the RdA.



237

238 **Figure 2. Sedimentological logs of selected cores with sedimentary facies recognised. Correspondence**  
 239 **with seismic units is shown in the left bars and architectural elements are noted to the right.**  
 240 **Radiocarbon ages (in cal a BP) from Table 1 are indicated in each core. See Fig. 1 for core location.**  
 241 **Depths are given in centimetres below seabed. C: clay; S; silt; fS; fine sand; mS; medium sand; cS:**  
 242 **coarse sand; G; gravel.**

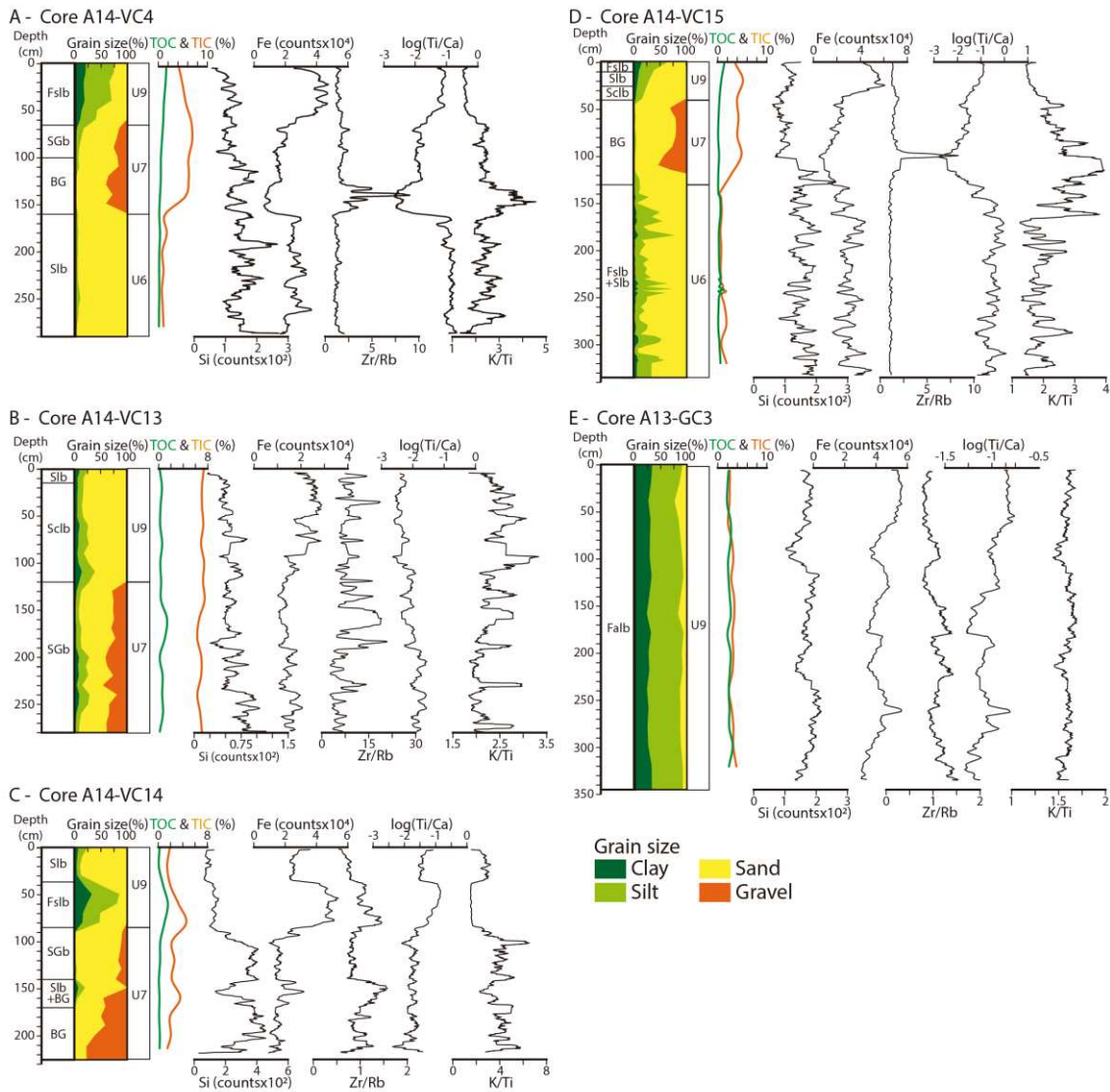
243

Facies	Description	Architectural elements	Top	Photograph	Base
BG	Grain-supported bioclastic gravels. Up to 15 cm diameter, composed mainly of bivalve shell fragments. Diffuse orientation of the clasts (parallel). Matrix of sand.	Tidal inlet Subtidal deposits Small-scale channel fills	VC4 148 cm		168 cm
SGb	Mixture of bioclastic gravels and coarse/very coarse sands. Aprox. 50% gravel and 50% sand. Matrix of mud. Composed mainly of bivalve shell fragments.	Storm fans Tidal inlet	VC4 98 cm		118 cm
Sc1b	Very coarse and coarse sand. Laminated. Sand fraction composed of quartz and bioclastic fragments. Abundant gravel-sized bioclastic fragments.	Storm fans Tidal inlet	VC14 108 cm		128 cm
Slb	Medium and fine sand. Laminated. Sand fraction composed of quartz and bioclastic fragments, with mm- and cm-scale bioclasts. Matrix of silt.	Tidal flats Small-scale channel fills	VC4 222 cm		242 cm
Fslb	Laminated sandy mud with gravel-sized bioclastic fragments. Composed of 20-50% of sand, <60% silt and <20% clay. Very high organic carbon content (TOC).	Subtidal deposits Small-scale channel fills	GC4 10 cm		30 cm
Falb	Laminated clayey silt with gravel-sized bioclastic fragments. Composed of <10% sand, >60% silt and >20% clay. Very high organic carbon content (TOC).	Subtidal deposits	GC1 10 cm		30 cm

244

245 **Figure 3. Description of main sedimentary facies. The enclosed photographs correspond to 20 cm intervals from cores, with an indication of depth ranges in each core**  
 246 **(distribution of facies along cores is shown in Fig. 4).**





247

248 **Figure 4. Diagram from five representative cores showing grain size distribution along cores, total**  
 249 **organic carbon (TOC) and total inorganic carbon (TIC) from elemental analysis and X-ray fluorescence**  
 250 **(XRF) profiles (in counts) for selected proxies (Si, Fe, Zr/Rb, Ti/Ca, and K/Ti) measured with the ITRAX**  
 251 **core scanner. Sedimentary facies and seismic units are also noted (detailed facies successions can be**  
 252 **found in Fig. 4). See text for methodology details and proxy interpretation. (A) Core A14-VC4; (B) core**  
 253 **A14-VC13; (C) core A14-VC14; (D) core A14-VC15; and (E) core A13-GC3. Depths are given in**  
 254 **centimetres below seabed.**

255

256

257

258

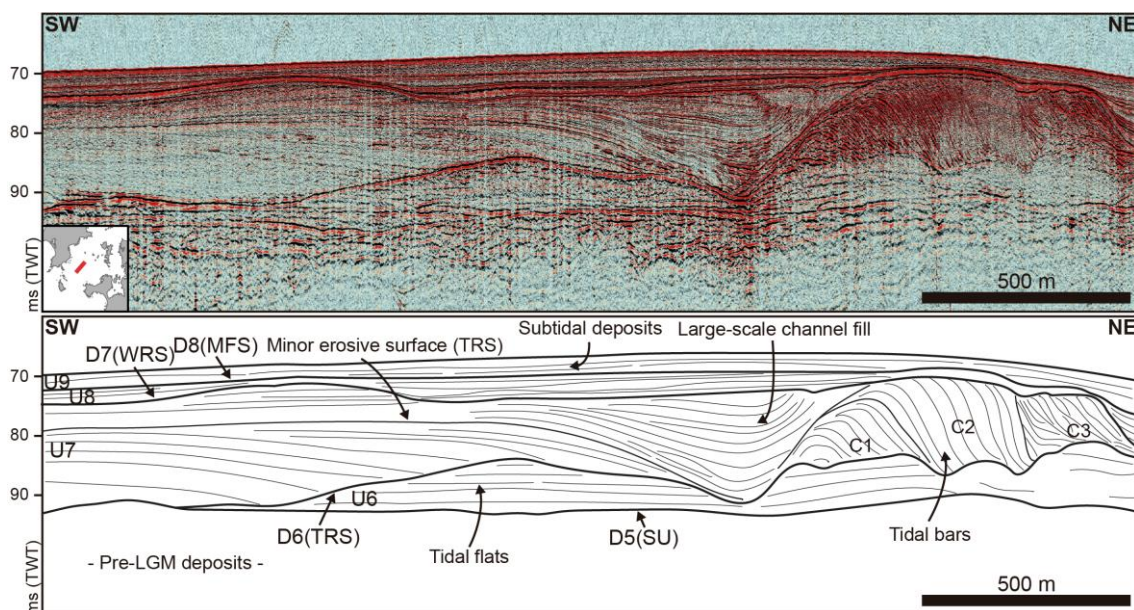
259

260 **4.3. Architectural elements and facies associations**

261 **4.3.1. Channel fills**

262 Channel fills were ranked according to their scale: large-scale (kilometre order),  
263 medium-scale (hundreds of metres) or small-scale (tens of metres).

264 *Large-scale channel fills* are mainly found as part of U7. Their outer shape generally  
265 displays a concave-up erosive base, with widths of kilometre order (0.5-1 km) and depths of 10  
266 to 25 m. Their infill corresponds to multiple phases of erosion and deposition, characterised by  
267 reflectors of high frequency, medium amplitude and generally high continuity (seismic facies  
268 sf2, Figs. 2 and 7). These channels appear commonly associated with tidal sand bars in the  
269 outer sector of the RdA (Fig. 7). Sedimentary facies were not recovered in the sediment cores.

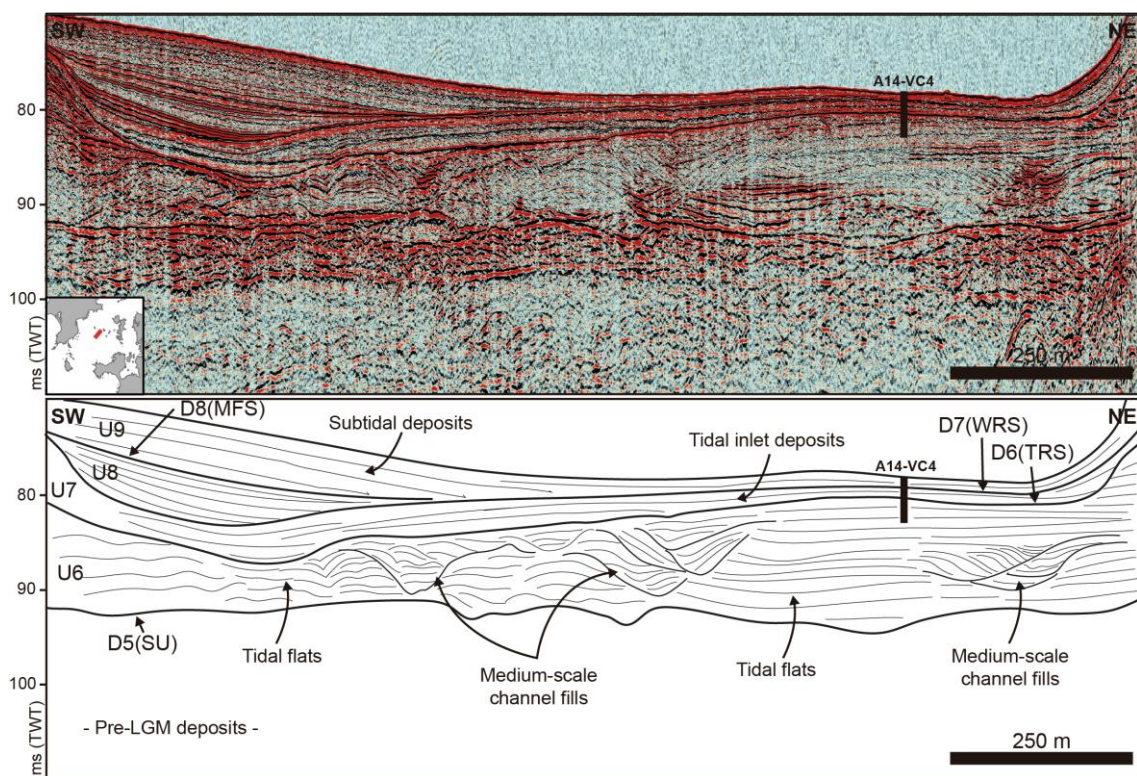


270

271 **Figure 5. Seismic profile and interpretation panel to illustrate the architectural elements recognized in**  
272 **the Ría de Arousa sedimentary fill. The tidal bar migrates to the NE, passing from sigmoidal to oblique**  
273 **configuration as the dipping angle of the clinoforms sets varies (C1, C2 and C3). Seismic units and main**  
274 **bounding surfaces are indicated. Location in inset maps. LGM: Last Glacial Maximum; SU: Subaerial**  
275 **Unconformity; TRS: Tidal Ravinement Surface; WRS: Wave Ravinement Surface; MFS: Maximum**  
276 **Flooding Surface; ms TWT: milliseconds two-way travel time.**

277 *Medium-scale channels* appear in the axial zone of the incised valley as part of U6 (Fig.  
278 8), to the south of the strait formed by the Rúa and Xidoiros islands (Fig. 1). They are

279 characterised by concave-up erosive bases with a V-shaped transverse profile, widths of 100 to  
 280 200 m and depths of 3 to 5 m, generally displaying an aggrading configuration. Their infill (Fig.  
 281 8) corresponds to several phases of erosion and deposition (cut-and-fill), but also channels  
 282 with lateral migration and vertical aggradation indicative of active channels with high spatial  
 283 mobility and relatively fast abandonment are recognised. Their seismic facies are generally  
 284 characterised by reflectors of high frequency and continuity and medium amplitude (sf1, Figs.  
 285 2 and 8). Sediments from these channels were not recovered in cores.

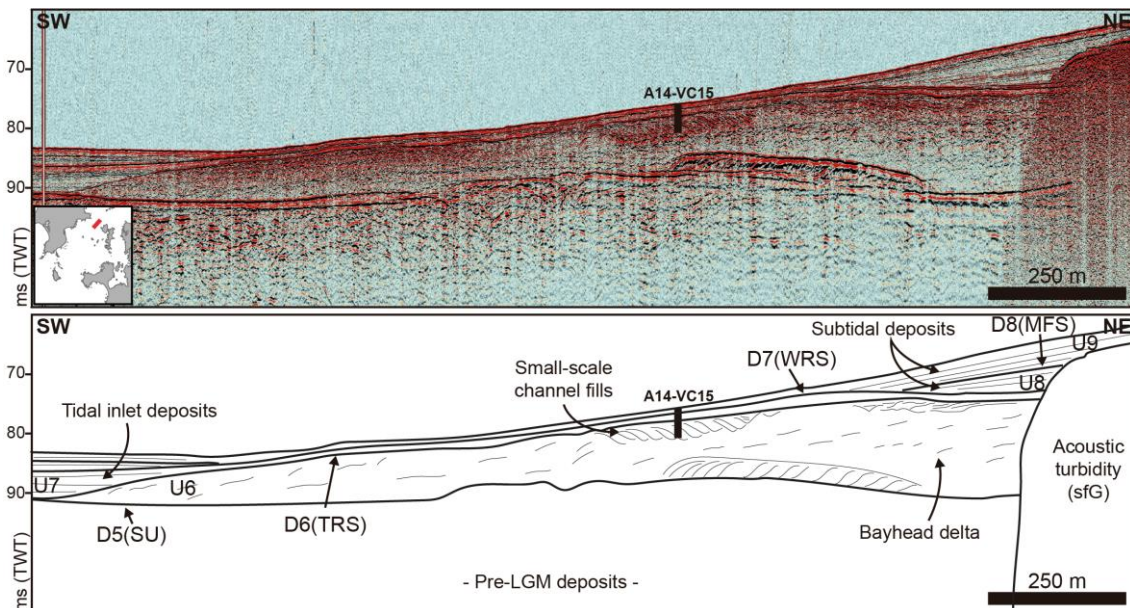


286

287 **Figure 6. Seismic profile and interpretation panel to illustrate the architectural elements recognized in**  
 288 **the Ría de Arousa sedimentary fill. Seismic units and main bounding surfaces are indicated. Location**  
 289 **in inset maps. LGM: Last Glacial Maximum; SU: Subaerial Unconformity; TRS: Tidal Ravinement**  
 290 **Surface; WRS: Wave Ravinement Surface; MFS: Maximum Flooding Surface; ms TWT: milliseconds**  
 291 **two-way travel time.**

292 *Small-scale channels* appear in both outer and inner sectors of the RdA, generally  
 293 towards the margins of U6 and U7. They are common within U6, appearing in the inner sector  
 294 in the upper part of a large-scale wedge-shaped sedimentary body (Fig. 9). In general, although  
 295 they show high variability, their vertical profile is V-shaped, less than 100 m wide and with  
 296 depths of up to 2 m. Their infill is parallel to the basal concavity, characterised by reflectors of

297 high continuity and frequency (sf1 and sf2, Fig. 2), onlap terminations and aggrading  
 298 configuration, commonly displaying lateral accretion (Fig. 9). Sedimentary facies of these  
 299 channels were recovered in vibrocore A14-VC15 (Figs. 4 and 9) and correspond to interbedded  
 300 beds of laminated mud (sedimentary facies Fslb, Fig. 5) and sand (sedimentary facies Slb, Fig.  
 301 5), also showing some beds of gravel-sized bioclastic fragments (Fig. 4). Elemental analysis (Fig.  
 302 6) indicates that these facies are characterised by low TIC and TOC (<1 % and <0.5 %, respectively),  
 303 with high Si and K/Ti values. The logarithmic Ti/Ca ratio shows negative values  
 304 close to zero (Fig. 6). Taken together, these proxies indicate a high terrestrial influence on the  
 305 source of these deposits, while the alternation of sandy and muddy beds (heterolytic bedding)  
 306 is typical of tidal environments. Palynological analyses, mainly including botanical microfossils,  
 307 performed on this core (García-Moreiras et al., 2019a) indicate mixed continental, freshwater,  
 308 brackish and marine influences.

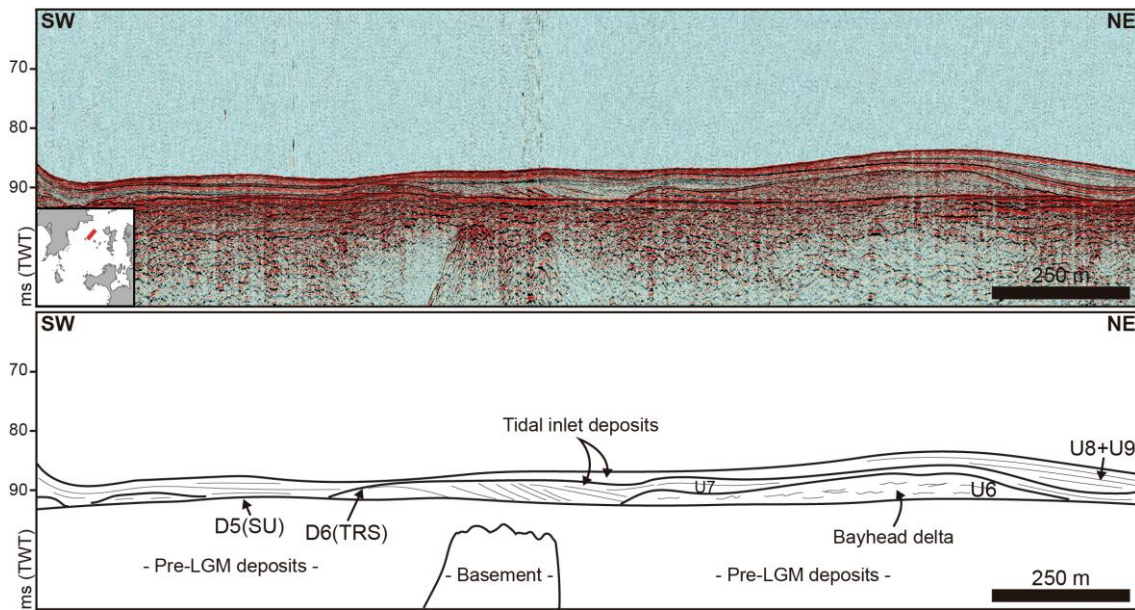


309

310 **Figure 7. Seismic profile and interpretation panel to illustrate the architectural elements recognized in**  
 311 **the Ría de Arousa sedimentary fill. Seismic units and main bounding surfaces are indicated. Location**  
 312 **in inset maps. LGM: Last Glacial Maximum; SU: Subaerial Unconformity; TRS: Tidal Ravinement**  
 313 **Surface; WRS: Wave Ravinement Surface; MFS: Maximum Flooding Surface; ms TWT: milliseconds**  
 314 **two-way travel time.**

315 **4.3.2. Tidal inlet**

316            This architectural element is identified associated with the submerged strait generated  
317 by the Rúa Island and the Xidoiros Islands (Fig. 1), where sedimentation is probably prevented  
318 by high-energy tidal currents, as deposits in this area are generally thin (Fig. 10). The inlet  
319 corresponds to a rock-bounded tidal inlet, examples of which were described elsewhere (e.g.  
320 Bertin et al., 2004; Chaumillon et al., 2008; Féliès et al., 2010; FitzGerald et al., 2005). The  
321 seismic character of sedimentary fills related to the tidal inlet is variable, with high amplitude  
322 reflectors infilling the base (sf1, Figs. 2 and 8), passing towards the top to more continuous  
323 seismic facies with less amplitude (sf2, Figs. 2 and 10). Sedimentary facies of this element of  
324 sedimentary architecture were recovered in several cores (A14-VC4, A14-VC14 and A14-VC15,  
325 Fig. 4). In general, a fining-upwards facies succession is identified, with thick basal deposits of  
326 bioclastic gravel (sedimentary facies BG, Figs. 4 and 5) passing upwards to laminated sandier  
327 (sedimentary facies Sglb and Slb, Figs. 4 and 5) and muddier facies (sedimentary facies Fslb,  
328 Figs. 4 and 5). Elemental analysis shows high values of TIC in the base (ca 6 %), decreasing  
329 towards the top (Fig. 6). Organic carbon increases from bottom to top (reaching values up to  
330 1.6 % TOC). XRF data shows marked decreases in the amount of Fe, with a sharp change in the  
331 logarithmic Ti/Ca ratio towards negative values (Fig. 6), indicating a high marine influence with  
332 lower terrestrial inputs, along with enrichment in coarse lithogenic material, as indicated by  
333 the Zr/Rb ratio.



334

335 **Figure 8. Seismic profile and interpretation panel to illustrate the architectural elements recognized in**  
 336 **the Ría de Arousa sedimentary fill. Seismic units and main bounding surfaces are indicated. Location**  
 337 **in inset maps. LGM: Last Glacial Maximum; SU: Subaerial Unconformity; TRS: Tidal Ravinement**  
 338 **Surface; WRS: Wave Ravinement Surface; MFS: Maximum Flooding Surface; ms TWT: milliseconds**  
 339 **two-way travel time.**

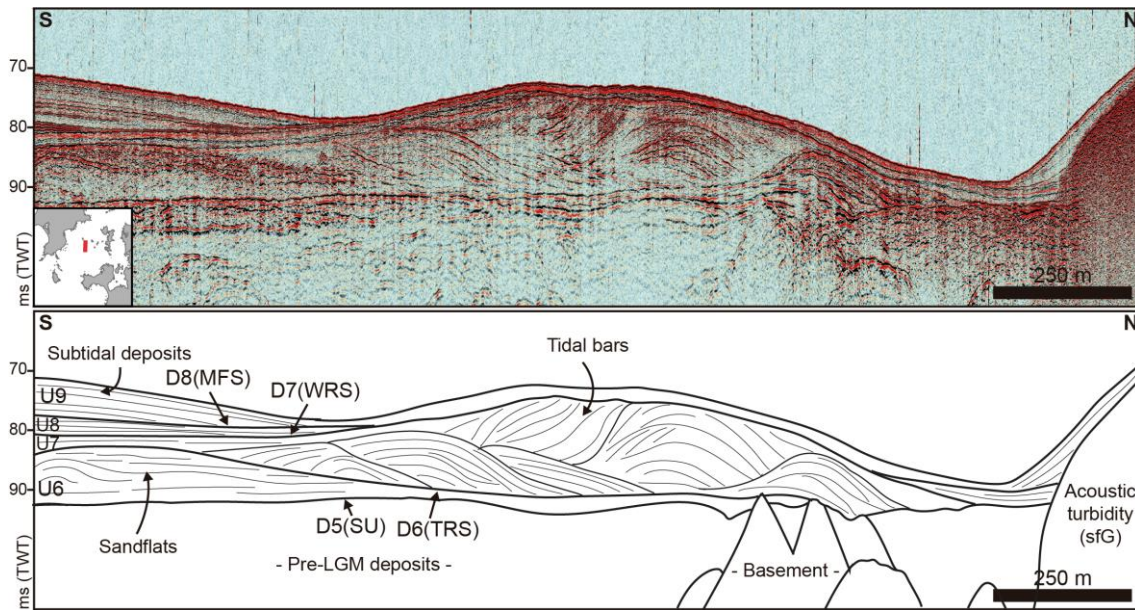
#### 340 4.3.3. Tidal flats

341 Tidal flats are identified in an axial position as part of U6 and in the basin margins as  
 342 part of U7 and U8. They represent thick tabular aggrading deposits (8-15 m) cut by small- and  
 343 medium-scale channels (Figs. 3 and 8), eroded at their top by disconformities D6 and D7.  
 344 Channel drainage system (of medium-scale channels) in axial tidal flats is mainly of braided  
 345 type. Their seismic facies are characterised by high-frequency reflectors, medium or high  
 346 amplitudes and variable continuity, probably denoting changes in the grain size of these  
 347 sediments (sf2, sf3 and sf5, Figs. 2, 3 and 8), and a degree of variability in its sedimentological  
 348 characteristics can be expected along the incised valley. However, sedimentary facies of tidal  
 349 flats were only recovered in the axis as part of U6, in vibrocore A14-VC4 (Fig. 4). These  
 350 correspond mainly to fine and very fine sands (>80 %, sedimentary facies Slb, Fig. 5) with  
 351 gravel-sized bioclastic fragments and parallel lamination. Elemental analyses show low values  
 352 for TIC and TOC (<1 % and <0.5 % respectively, Fig. 6). XRF data indicate high Fe and Ti/Ca ratio  
 353 values that, although negative, approach zero (Fig. 6). As a whole, these proxies indicate that,

354 although marine influence on the origin of sediments is high, terrestrial contribution is  
355 relevant.

#### 356 **4.3.4. Tidal sand bars**

357 Tidal sand bars are prograding sedimentary bodies mainly identified within U7 (Figs. 3  
358 and 11), towards the outer sector, infilling large erosional depressions of surface D6 and  
359 usually associated with large-scale channel fills (Fig. 7). Dimensions are variable, as well as  
360 their prograding directions. Tidal sand bars are characterised by sigmoidal to oblique  
361 prograding configuration and downlap terminations (sf6, Fig. 2). Accretion surfaces are lateral  
362 to oblique to the tidal currents. The migration direction, although complex, is generally  
363 landwards (Fig. 12A). Towards the outermost areas, tidal sand bars appear in a basal  
364 stratigraphic position within U7, confined to incisions of surface D6 and represent lenticular  
365 deposits with thicknesses of up to 10 m and more than 1 km wide (Fig. 3). Tidal sand bars also  
366 occur slightly landwards in the valley axis associated with large-scale channels (Fig. 7) and to  
367 the south of the strait (Fig. 11). They display mounded shapes, resting on a subhorizontal  
368 erosive basal surface, reaching thicknesses of up to 13 m. Their top is disconformity D7. The  
369 example shown in figure 7 has a slightly elongated shape in plan view (Fig. 12A), 800 m long  
370 and 500 m wide. The migration of this body is noticed by clinoforms sets (C1, C2 and C3, Fig. 7)  
371 that migrate in an oblique direction to the valley axis displaying variable angles of stratification  
372 and thicknesses. Low-angle mounded clinoforms sets are identified at the base (C1), above  
373 which clinoforms sets with a greater dipping angle and an oblique configuration are recognised  
374 (C2). Younger clinoforms sets (to the northwest in figure 7, C3) have a lower dipping angle,  
375 with oblique configuration, and represent thin lenticular deposits (ca. 3 m). Figure 11 shows  
376 another example of this type of tidal sand bars, with lenticular geometry, where basal mounds  
377 constitute the nucleus of the tidal sand bars, which progressively migrate to the north.



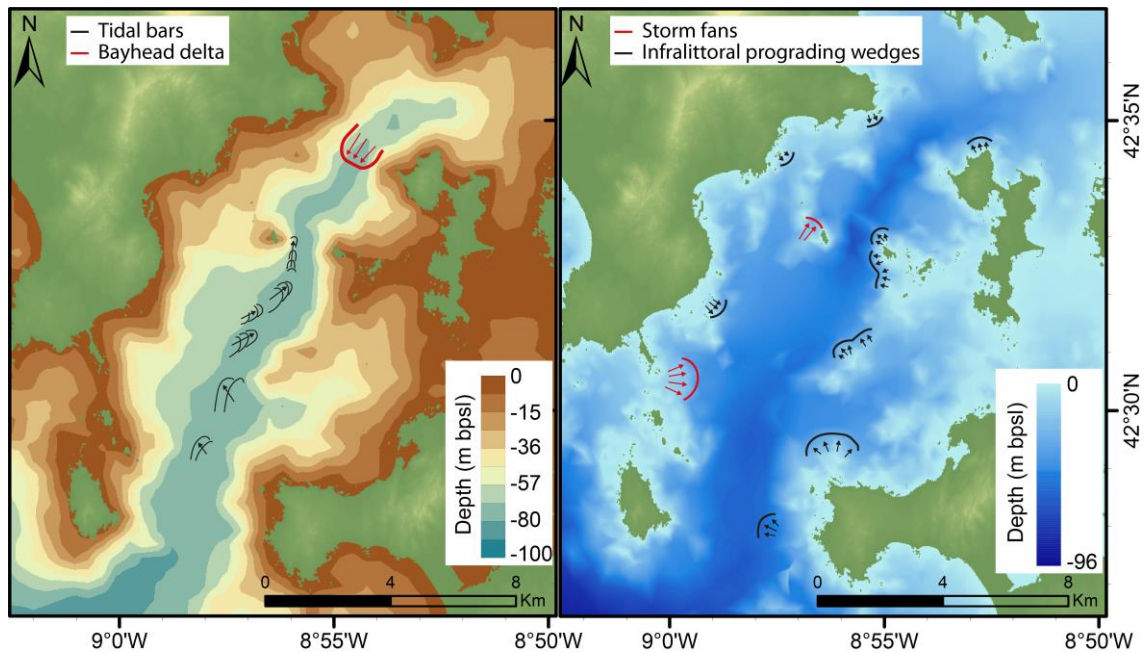
378

379 **Figure 9. Seismic profile and interpretation panel to illustrate the architectural elements recognized in**  
 380 **the Ría de Arousa sedimentary fill. Seismic units and main bounding surfaces are indicated. Location**  
 381 **in inset maps. LGM: Last Glacial Maximum; SU: Subaerial Unconformity; TRS: Tidal Ravinement**  
 382 **Surface; WRS: Wave Ravinement Surface; MFS: Maximum Flooding Surface; ms TWT: milliseconds**  
 383 **two-way travel time.**

#### 384 4.3.5 Infralittoral prograding wedges

385 Infralittoral prograding wedges (IPWs sensu Hernández-Molina et al., 2000) are  
 386 sedimentary bodies identified as part of the youngest seismic unit in the RdA (U9), located on  
 387 the basin margins (Fig. 3). These deposits are composed of several groups of clinoforms with  
 388 oblique to sigmoidal prograding configurations (sf6, Fig. 2) resting on a subhorizontal basal  
 389 downlap surface, disconformity D8, slightly dipping seaward. Bedding planes of these  
 390 clinoforms show higher angles towards the deeper zones as the sedimentary body advances  
 391 towards the axis of the ria. They are characterised by thicknesses of up to 10 m and 500-800 m  
 392 in length with a wedge geometry. IPWs are common in the outer sector of the RdA, parallel to  
 393 the coastline, and associated with smaller islands such as the Xidoiros Islands (Fig. 12B). Their  
 394 sedimentary facies were not recovered in the cores; however, surface sediment mapping of  
 395 the RdA (Koldijk, 1968; Vilas et al., 2005) indicate that they are restricted to sandy and gravelly  
 396 areas.





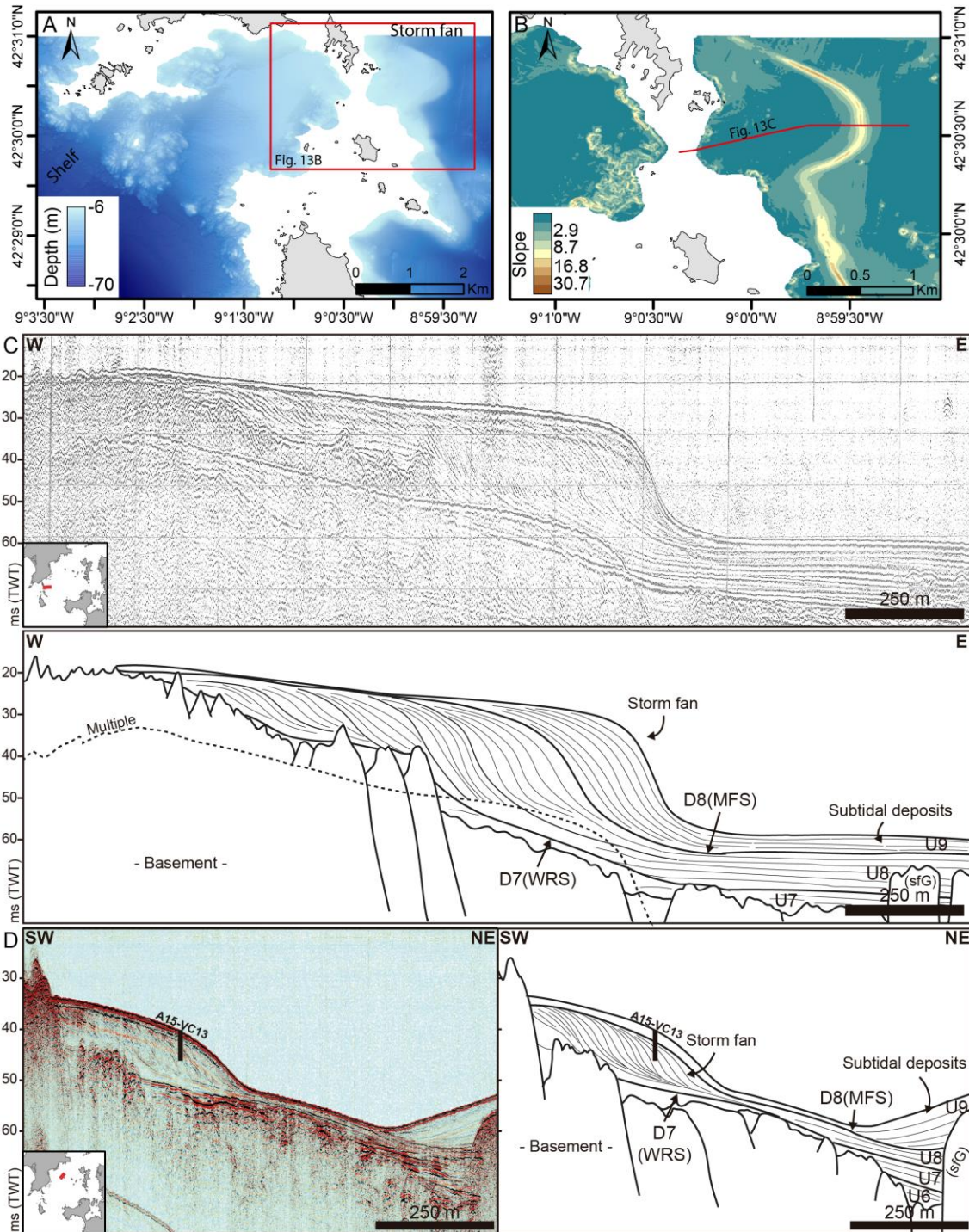
397

398 **Figure 10. (A) Coloured contour map of disconformity D5 (subaerial unconformity of the Last Glacial**  
 399 **Maximum) in meters below present sea level (m bpsl). Mapping of tidal sand bars, in black, (U7) and**  
 400 **bayhead delta, in red, (U6) also included. (B) Map of storm fans, in red, (U8 and U9) and infralittoral**  
 401 **prograding wedges, in black, (U9). The background corresponds to present-day bathymetry in meters**  
 402 **below present sea level.**

403 **4.3.6. Storm fans**

404 Storm fans associated with structural basement highs (sensu Martínez-Carreño et al.,  
 405 2017) are large prograding sedimentary bodies that migrate landwards and appear as part of  
 406 U8 and U9, always associated with a rocky barrier generated by topographic highs of the rocky  
 407 basement (Fig. 13). These deposits are always located in the protected zone behind structural  
 408 highs, growing landward with wedge geometries in cross-section and fan morphologies in plain  
 409 view, characterised by seismic facies sf6 (Fig. 2). Based on the available data, three prograding  
 410 bodies of this type have been identified and mapped in the RdA (Fig. 12B), but there may be  
 411 more associated with the numerous basement topographic highs occurring in the ria (Fig. 1).  
 412 The sedimentary body associated with the islands around Sálvora features a symmetrical fan  
 413 morphology in plan view, which disperses from the passage between the islands (Fig. 13A, B).  
 414 Its internal structure shows several groups of oblique to sigmoidal clinoforms. The clinoforms  
 415 rest above disconformity D7, overlying basal deposits characterised by bedding planes with

416 minor slopes that are part of U7. This group of clinoforms build up the majority of the  
417 sedimentary body. The groups of younger clinoforms, as part of U9, show bedding planes with  
418 higher dipping angles, downlapping surface D8 (Fig. 13C). Maximum thickness is 30 m, with the  
419 prograding body extending 1.3 km and thinning landwards, where the storm fan passes  
420 laterally to subtidal deposits. Sedimentary facies of this body were not recovered, although  
421 surface sediment corresponds mainly to coarse sand and bioclastic gravel (Vilas et al., 2005).  
422 Another similar body has been identified to the northwest of the Rúa Island, associated with a  
423 submerged basement high (Fig. 13D). Although its plan morphology has not been mapped  
424 accurately, it displays a more asymmetrical, wedge-shaped elongated geometry trapped  
425 between the basement highs that flank the Rúa Island (Fig. 12B). Its internal structure shows  
426 several clinoforms sets, sigmoidal to oblique, that migrate landwards (towards the northeast in  
427 Fig. 13D). Dipping of bedding planes is also variable, being of lower angle in the oldest  
428 clinoforms sets, the nucleus of the body, and higher in the younger ones. This body progrades  
429 above surface D7, a subhorizontal erosive disconformity. Sedimentary facies of this body were  
430 recovered in vibrocore A14-VC13, corresponding fundamentally to gravel-sized bioclastic  
431 sediments and coarse sands. A general finning-upward succession is identified (Fig. 4), with  
432 basal beds of gravel and coarse and very coarse bioclastic sands (sedimentary facies SGb, Fig.  
433 5), passing upwards to laminated coarse sands (sedimentary facies Sclb, Fig. 5), and finally, to  
434 fine and medium sands with high angle lamination (sedimentary facies Slb, Fig. 5). Elemental  
435 analysis shows high carbonate content ( $TIC > 8\%$ , Fig. 6) and low organic carbon content  
436 ( $TOC < 1\%$ , Fig. 6), while XRF proxies denote a marine source (Fig. 6).



437

438 Figure 11. (A) Multibeam bathymetry (Spanish Ministry of Agriculture, Fishing and Food - MAPAMA)  
 439 obtained in the northern mouth of the Ría de Arousa showing a storm fan. (B) Detailed slope map in  
 440 the area of the storm fan. (C) Seismic profile and interpretation panel through the storm fan of A and  
 441 B. (D) Seismic profile and interpretation panel through the storm fan in the inner sector of the Ría de  
 442 Arousa (see inset map for location). LGM: Last Glacial Maximum; SU: Subaerial Unconformity; TRS:  
 443 Tidal Ravinement Surface; WRS: Wave Ravinement Surface; MFS: Maximum Flooding Surface; ms  
 444 TWT: milliseconds two-way travel time.

445 **4.2.7. Bayhead delta**

446           Towards the inner sector of the RdA, as part of U6, a sedimentary body with a wedge  
447 geometry is recognised (Fig. 9). It is characterised by almost chaotic seismic facies (sf5, Fig. 2)  
448 with reflectors of low continuity and high amplitude, although a prograding configuration can  
449 be inferred (Fig. 9). These deposits are thick landwards (>16 m) and become thinner seawards,  
450 although the maximum thickness cannot be determined due to the presence of extensive  
451 acoustic turbidity areas towards the innermost areas (sfG, Fig. 9). In its upper part, this body is  
452 reworked by small-scale channels. This body corresponds to bayhead delta deposits that  
453 disperse from the inner sector towards the strait, encased between relative topographic highs  
454 of the rocky basement and limited at their top by disconformity D6, which erodes this body  
455 seawards (towards the southwest in Fig. 9). Sedimentary facies of this architectural element  
456 were not recovered.

#### 457 **4.3.8. Subtidal deposits**

458           This sedimentary architectural element includes all the subtidal deposits that  
459 dominate the present-day seafloor of the RdA (U8 and U9) with a sheet drape geometry. In the  
460 seismic records, they are characterised by parallel or subparallel reflectors of medium to high  
461 frequency with variable continuity, generally with medium amplitude (sf2, Fig. 2), although  
462 sometimes reflectors of higher amplitude and continuity are present (sf3, Fig. 2). These  
463 deposits are also affected by extensive acoustic turbidity (sfG, Figs. 2 and 9), particularly in the  
464 innermost areas of the RdA and in the north-western margin of the outer sector. Gravity cores  
465 recovered sedimentation from protected areas under low-energy conditions and show a  
466 predominance of laminated mud (facies Fslb and Falb, Fig. 5), rich in organic matter (2-4% TOC,  
467 Fig. 6), a low proportion of carbonates (<4% TIC, Fig. 6) and abundant plant remains.  
468 Interbedded levels of bioclastic gravel (facies BG, Fig. 5) towards the base of the cores (Fig. 4)  
469 are also recognised, denoted in the seismic records by seismic facies sf3.

## 470 **5. Discussion**

## 471 **5.1 Palaeogeographical reconstruction**

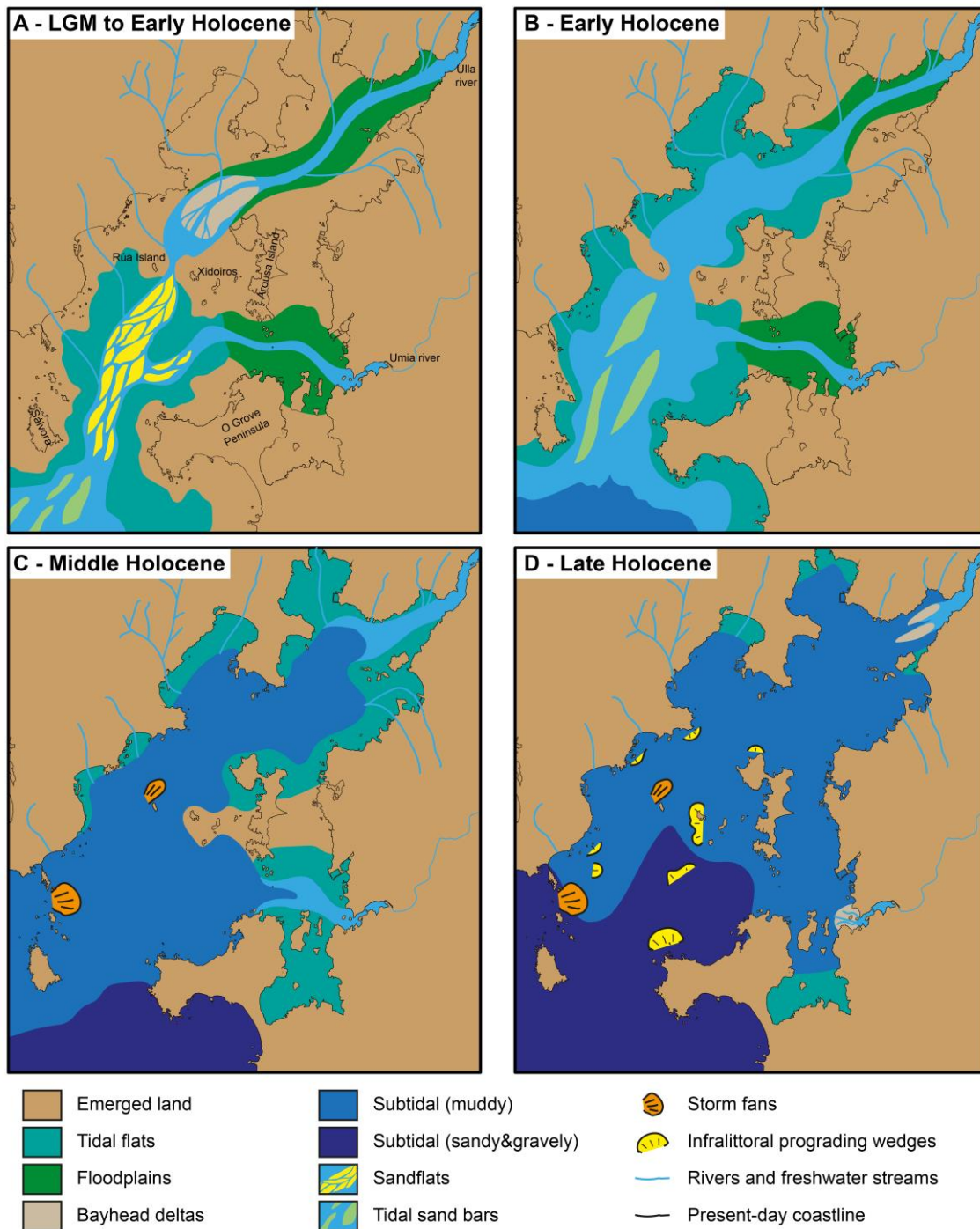
472 The combined analysis of high-resolution seismic profiles and sedimentary facies  
473 allowed us to identify several elements of sedimentary architecture that can be used to  
474 reconstruct the palaeogeographical evolution of the submerged areas of the RdA during the  
475 postglacial period (Fig. 14). The succession of facies records an overall transgression, in which  
476 the migration of the coastline and the depositional environments within the incised valley has  
477 been controlled by the interaction of global and regional factors (sea-level rise, physiography,  
478 hydrography, sediment source...).

### 479 **5.1.1 Last Glacial Maximum to Early Holocene (20-11.7 ka BP)**

480 Climatic degradation during the last glaciation resulted in a marked fall in global sea  
481 level that reached a position of -130 m below the present level during the LGM (e.g.  
482 Austerman et al., 2013; Lambeck et al., 2014). This led to the subaerial exposure of the entire  
483 RdA, with an intense episode of erosion (that is reflected by disconformity D5) and the fluvial  
484 incision of a wide valley. This palaeovalley was limited in the southeast margin by the relative  
485 topographic highs of the rocky basement and the northwest margin by deposits from previous  
486 sequences (Figs. 3 and 12A). Surface D5, therefore, corresponds to a subaerial unconformity  
487 (SU, Sloss et al., 1949; Zecchin and Catuneanu, 2013). Deposits from the lowstand (LST) are not  
488 preserved or are very thin at the base of U6 and cannot be clearly distinguished from other  
489 overlying deposits, so the nature of the drainage system that was established cannot be  
490 investigated. This also occurs in the nearby Ría de Vigo (Fig. 1), where thin fluvial lowstand  
491 deposits were only recovered at the base of some cores but were not clearly distinguished in  
492 seismic data (Martínez-Carreño, 2015; Martínez-Carreño and García-Gil, 2017). However,  
493 palaeotopography of D5 (Fig. 12A) shows a low-slope surface where a single valley can be  
494 distinguished. This surface runs along the axial zone of the RdA, which was probably drained by

495 a fluvial system. This valley has a branch to the east of the basin marking the possible junction  
496 point of the Umia river as a tributary (which currently flows into the RdA in the east, Fig. 1).

497 Unit U6 represents transgressive deposits of the postglacial sea-level rise and is  
498 interpreted as a transgressive system tract (TST) given its aggrading character and onlap  
499 terminations. The radiocarbon data obtained in the inner sector, in core A14-VC15 (Fig. 4),  
500 indicates that marine influence was already significant at 13450-14500 cal a BP (Fig. 4). This  
501 dating was obtained from shells present in tidal sediments at a depth of approximately -64 m  
502 below present sea level and is related to the high rates of sea-level rise during the postglacial.  
503 A significant marine influence is also supported by the presence of relatively high fluxes of  
504 marine microfossils in these sediments, with dinoflagellate cysts and foraminiferal linings  
505 reaching accumulation rates of  $1150 \text{ cysts}\cdot\text{cm}^{-2}\cdot\text{a}^{-1}$  and  $160 \text{ microremains}\cdot\text{cm}^{-2}\cdot\text{a}^{-1}$ , respectively  
506 (Garcia-Moreiras et al., 2019a). The high rates of sea-level rise at the beginning of the  
507 postglacial period are related to melt-water pulse 1A (MWP-1A), which occurred after 14.6 cal  
508 ka BP (Deschamps et al., 2012). The flooding of the RdA turned the valley into a large estuary,  
509 where the thick deposits of U6 accumulated. Wide tidal flats appear in the margins of the  
510 central valley (Figs. 3 and 14A), as occurs in most tide-dominated estuaries (Chaumillon et al.,  
511 2010; Dalrymple et al., 2012, 1992; Dalrymple and Choi, 2007; Tessier, 2012), both in the outer  
512 and inner segments.



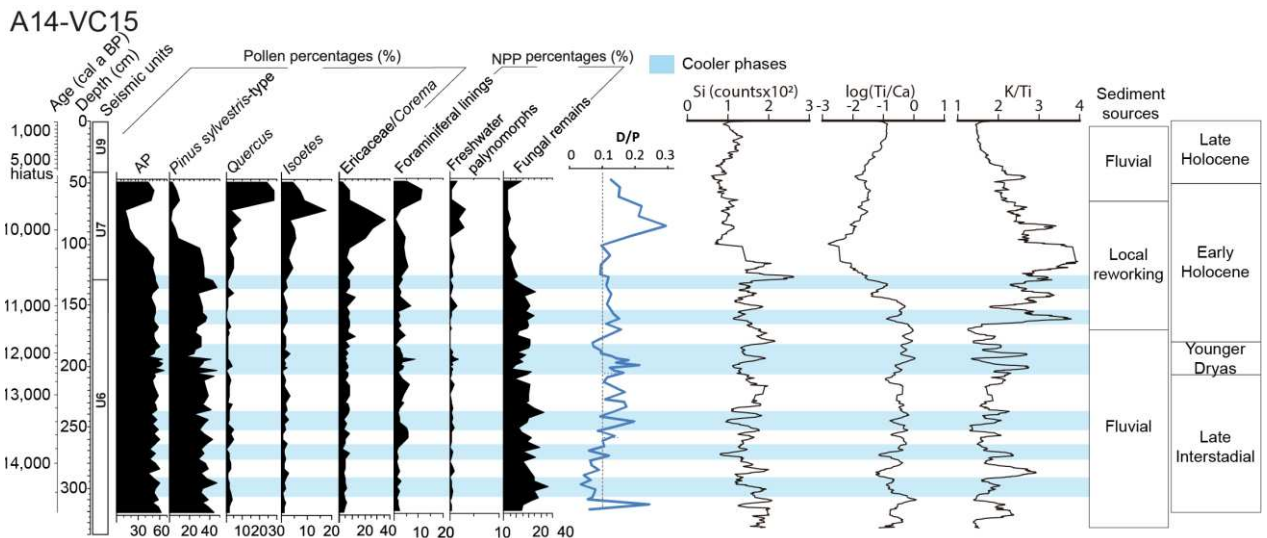
513

514 **Figure 12. Palaeogeographic evolution of the Ría de Arousa since the Last Glacial Maximum [LGM]. (A)**  
 515 **LGM to Early Holocene, the incised valley was mainly a tide-dominated estuary; (B) Early Holocene,**  
 516 **the elements of a tide-dominated estuary migrated landwards; (C) Middle Pleistocene, due to the**  
 517 **progressive flooding the incised valley turned into a wave-dominated estuary; and (D) Late**  
 518 **Pleistocene, wave-dominated estuary with extensive progradation in the basin margins.**

519 The innermost part is occupied by a thick bayhead delta (Figs. 9, 12 and 14A), where  
 520 fluvial sediments from the Ulla river accumulated. These deposits are thinner towards the  
 521 palaeo-strait, partially eroded at their top by disconformity D6. Fluvial deposits were probably

522 trapped in this inner area induced by the rocky barrier formed by the relative topographic  
523 highs of the basement. The bayhead delta deposits are older than 14 cal ka BP, as indicated by  
524 radiocarbon dates of core A14-VC15 (Fig. 4). Its seismic facies (sf4, Fig. 2), with an almost  
525 chaotic configuration, high amplitude and low continuity reflectors, is interpreted as the  
526 acoustic attributes of coarse-grained continental deposits (gravel or sand). This facies is similar  
527 to fluvial and bayhead delta facies identified in other incised valleys (e.g. Bahr et al., 2005;  
528 Greene et al., 2007; Simms et al., 2010; Tesson et al., 2015). Additionally, deposits of the RdA  
529 interpreted as a bayhead delta have similar dimensions to the bayhead deltas described by  
530 Aschoff et al. (2018). At its top, the bayhead delta of the RdA is reworked by small-scale  
531 channels (Fig. 9), with a clear tidal influence, as reflected by the heterolithic bedding found in  
532 core A14-VC15 (Fig. 4). Geochemical proxies (Fig. 6) denote a high terrestrial influence on the  
533 source of these sediments so that they can be attributed to the inner segment of an estuary.  
534 Palynological analyses by García-Moreiras et al. (2019a) also point to mixed sources of  
535 microremains (marine, terrestrial and brackish), as indicated by the low D/P ratio and the  
536 occurrence of marine (dinoflagellate cysts and foraminiferal linings) and terrestrial (fungi and  
537 pollen) microfossils (Fig. 15). Deposits of these small-scale channels show a general aggrading  
538 configuration, with multiple phases of erosion and infill, which is consistent with the  
539 transgressive context in which they were developed. In addition, they migrate to  
540 topographically higher areas (e.g. the channel on which core A14-VC15 was recovered, Fig. 9),  
541 probably due to the progressive marine flooding of the area. The described heterolithic facies,  
542 with interbedded laminae of mud and sand (sedimentary facies Fslb and Slb, Figs. 4 and 5), are  
543 frequently found in estuaries of macrotidal coasts (e.g. Tessier, 2012; Tessier et al., 2010a,  
544 2010b) and tidal bars are common as part of estuarine bayhead delta deposits (Allen, 1991;  
545 Allen and Posamentier, 1993; Billy et al., 2012; Chaumillon et al., 2013; Dalrymple et al., 1992)  
546 associated with multiple distributary channels (Aschoff et al., 2018).





547

548 **Figure 13. Diagram of percentages of pollen and NPP (non-pollen palynomorphs) types, D/P ratio (the**  
 549 **ratio of dinocyst to pollen+spores+dinocyst count), and elemental data (Si, log(Ti/Ca) and K/Ti from**  
 550 **ITRAX core scanner) for core A14-VC15. The interpretation of sediment sources is also indicated,**  
 551 **based on the K/Ti ratio. Age model and cooler phases from García-Moreiras et al. (2019a). Depths are**  
 552 **given in centimetres below seabed. AP: total tree pollen.**

553           Toward the outer areas of the valley, to the south of the palaeo-strait (Rúa Island –  
 554 Xidoiros, Fig. 14A), thick deposits of sandy tidal flats (Fig. 8) are preserved with similar ages (ca.  
 555 13 cal ka BP, Fig. 4) to that of the bayhead delta. Core A14-VC4 (Fig. 4) recovered sandy facies  
 556 (fine and very fine sand, sedimentary facies Slb, Fig. 5) with parallel lamination, indicating  
 557 medium to high energy conditions. These sandflats were drained by a system of medium-scale  
 558 channels of low sinuosity (braided type, Fig. 8). The seismic and sedimentary facies and the  
 559 geometry of these deposits are similar to the high-energy sandflats typical of the middle  
 560 segment of tide-dominated estuaries (upper-flow-regime sandflats, Dalrymple et al., 2012,  
 561 1992; Dalrymple and Choi, 2007). These deposits denote the zone of greatest tidal energy,  
 562 located in the transition from the outer estuary to the inner estuary. In the RdA, the location of  
 563 the tidal maximum is possibly influenced by the strait, where the compression of the tidal  
 564 prism may increase velocities of tidal currents, particularly during the ebb, additionally  
 565 increased by the contribution of fluvial currents, compressed in front of the bayhead delta.

566           Towards the outermost areas of the valley, preservation of U6 is limited as it is deeply  
 567 eroded by surface D6 (Fig. 3). However, this area was probably occupied by bars associated

568 with tidal channels and scours of the sandflats (Fig. 14A), intensely reworked during  
569 transgression, as commonly found in the outer sector of tide-dominated estuaries (Dalrymple  
570 et al., 2012, 1992; Dalrymple and Choi, 2007).

### 571 **5.1.2 Early Holocene (11.7-8 ka BP)**

572 The beginning of the Early Holocene is characterised by a period of higher energetic  
573 conditions and intense erosion on some sectors of the incised valley leading to the formation  
574 of disconformity D6 (Fig. 3). This surface is interpreted as a tidal ravinement surface (TRS, Allen  
575 and Posamentier, 1994; Catuneanu et al., 2011; Dalrymple et al., 1992) as it is closely related  
576 to tidal deposits (Fig. 3). The generation of a ravinement surface involves a substantial erosion,  
577 from meters to tens of meters, with an intense reworking of the previous deposits (Cattaneo  
578 and Steel, 2003; Zecchin and Catuneanu, 2013). Transgressive deposits of U7 overlying D6  
579 record the Early Holocene, between ca. 11 and 8 cal ka BP (Fig. 4). The progressive flooding of  
580 the RdA caused the tidal prism to move towards inner and shallower areas. The strait turned  
581 into a tidal inlet bounded by the rocky basement relative topographic highs (Figs. 8, 10 and  
582 14B), controlling the hydrodynamics in the estuary by compressing the flow, accelerating tidal  
583 currents and intensifying erosion. Deposits are mainly coarse sediments, with bioclastic sand  
584 and gravel, a consequence of the high tidal energy (sedimentary facies BG, Figs. 4 and 5). Rock-  
585 bounded tidal inlets were described in numerous estuaries of the European Atlantic coast,  
586 causing a marked tidal erosion and even preventing present-day sedimentation (e.g.  
587 Chaumillon and Weber, 2006; Féliès et al., 2010). The high tidal energy in the RdA is probably  
588 maintained at present, as the strait is still clearly identified in the axis of the RdA. However, in  
589 cores recovered in this tidal inlet (e.g. A14-VC4 and A14-VC14, Fig. 4), a fining-upwards  
590 sedimentary succession is recognised that points to a progressive decrease in energy, perhaps  
591 a consequence of the increase in the water column as the transgression proceeded. In the  
592 inner sector, the bayhead delta is no longer active, and tidal erosion dominates (Fig. 9). These

593 deposits probably retreated towards innermost areas, but its investigation is prevented by  
594 extensive acoustic turbidity (Fig. 9). Pollen data indicates that heaths, coastal meadows,  
595 marshes and other hygrophilous ecosystems characteristic of supratidal environments were  
596 probably extensive in the innermost and shallower areas (Fig. 15, García-Moreiras et al.,  
597 2019a).

598           During the Early Holocene, the outer sector of the RdA is occupied by large subtidal  
599 channels and tidal sand bars developed in the axis (Figs. 3, 7, 11 and 14B). According to their  
600 internal structure and morphology, these features correspond to type 2A tidal sandbanks  
601 (sand ridges) as per the classification of Dyer and Huntley (1999), which are common in the  
602 mouth of tide-dominated estuaries (Dalrymple et al., 2012, 1992; Dalrymple and Choi, 2007).  
603 These sedimentary bodies migrated landwards (Fig. 12A) following the sea level transgressive  
604 trend associated with large-scale channel fills (Fig. 7). The direction of landwards-dominant  
605 migration reconstructed for these bodies indicates development mainly in a subtidal  
606 environment, with a predominance of flood tidal currents (Fig. 14B). Within U7, several  
607 subunits have been characterised, bounded by minor erosive discontinuities that are only  
608 locally identified. These subunits result from the landward migration of the tidal sand bars and  
609 large-scale channel systems, producing minor surfaces of ravinement erosion, which can also  
610 be interpreted as TRSs (Figs. 3 and 7). Extensive tidal flats flanked these deposits, with thick  
611 aggrading deposits (Figs. 2 and 14B).

612           As the tidal sand bars approached the strait (Rúa Island-Xidoiros, Figs. 1 and 14B), its  
613 internal structure becomes more complex (Figs. 7 and 11). Migration and accretion of these  
614 bodies were probably controlled by the complex hydrodynamics caused by the presence of the  
615 (now submerged) palaeo-strait. Considering its complex internal structure, variable in time and  
616 with accretion planes generally oblique to the main direction of the tidal current, and its  
617 mounded geometry, these bodies are also similar to the type 3A (banner banks) of Dyer and

618 Huntley (1999), and probably consequence of a similar formation process. The origin of this  
619 type of tidal sandbanks is related to the presence of vortices generated by the asymmetry of  
620 tidal flows as a consequence of structural highs (headlands, Bastos et al., 2004; Berthot and  
621 Pattiaratchi, 2006; Dyer and Huntley, 1999), which in the case of the RdA is consequence of  
622 the location of the palaeo-strait.

### 623 **5.1.3 Middle and Late Holocene (8 ka BP to present)**

624 The Middle Holocene marks a change in the stratigraphic architecture of RdA infill,  
625 denoting transition from an environment dominated by tidal processes (units U6 and U7, Fig.  
626 14) to a predominance of wave processes (units U8 and U9, Fig. 14). This change in the  
627 dominant processes within the basin allows us to interpret disconformity D7 as a wave  
628 ravinement surface (WRS, Catuneanu et al., 2011; Demarest and Kraft, 1987; Nummedal and  
629 Swift, 1987; Swift, 1968). The available radiocarbon dates (Fig. 4) indicate that this  
630 disconformity (D7) was generated between 8700-9590 cal a BP (top of U7) and 6435-7225 cal a  
631 BP (base of U8). Lower rates of sea-level rise rates after 8 ka (Costas et al., 2016) led to limited  
632 accommodation, and along the basin margins storm fan progradation began as part of U8  
633 (Figs. 13 and 14C). The prograding clinoforms sets of these bodies pass laterally to the subtidal  
634 deposits in the bottomset (Fig. 13C), with both types of deposits overlying the WRS (D7). The  
635 growth model of this type of storm fans, associated with rocky barriers and migrating  
636 landwards (from the shelf to the ria), was proposed by Martínez-Carreño et al. (2017) from the  
637 study of a similar body in the Ría de Vigo (Fig. 1), associated with the Cíes Islands barrier. The  
638 origin of these bodies is related to sediment transport carried by storm waves, which on the  
639 northwest coast of Iberia come mainly from the southwest and have the capacity to mobilise  
640 sediments from the shelf (Vitorino et al., 2002a, 2002b). These sediments are transported  
641 towards the interior of the incised valleys, being deposited behind the rocky barriers of the  
642 islands and forming the prograding fans (Figs. 13 and 14C). Genesis and preservation of these

643 storm fans is a consequence of the equilibrium between accommodation (linked to low rates  
644 of relative sea-level rise) and sediment supply during the Middle and Late Holocene. Towards  
645 the inner sector of the RdA, a similar body formed close to Rúa Island (Figs. 12B, 13D and 14C),  
646 whose origin can be attributed to the same process: the transport of sediments eroded from  
647 the seabed of the valley by storm waves later trapped at the back of a local topographic high.  
648 Core A14-VC13 (Fig. 4) shows a coarse bioclastic lithology, with a predominance of coarse sand  
649 and gravel grain sizes (sedimentary facies SGB, SCLB and SLB, Figs. 4 and 5), which supports an  
650 origin by high-energy processes. XRF data indicates that the sediment is primarily of marine  
651 origin (negative logarithmic Ti/Ca ratio values, Fig. 6) and the Zr/Rb ratio (Fig. 6) indicates an  
652 alternation of beds enriched in coarse lithogenic material (high Zr/Rb, Rothwell and Croudace,  
653 2015) and beds with higher clay content (low Zr/Rb, Rothwell and Croudace, 2015).

654         The base of the most recent seismic unit of the RdA (surface D8, base of U9) denotes  
655 the beginning of the generalised progradation of sedimentary bodies on the basin margins,  
656 with IPWs migrating towards the axis of the incised valley (Figs. 3 and 12B). Surface D8 is,  
657 therefore, interpreted as the maximum flooding surface (MFS, Catuneanu et al., 2011;  
658 Posamentier and Vail, 1988; Van Wagoner et al., 1988), associated with a lower rate of relative  
659 sea-level rise (Costas et al., 2016; Leorri et al., 2012). IPWs appear as isolated bodies generally  
660 below the wave base (below 25 m in the RdA), and their growth is produced by the seaward  
661 sediment transport from shallower areas as a consequence of strong littoral currents. These  
662 bodies are located parallel to the coastline, migrating toward deeper waters (Figs. 12B and  
663 14D).

664         During the Middle and Late Holocene in the central areas of the RdA the rock-bounded  
665 tidal inlet remains active (Figs. 10 and 14D), even though the slow but continuous rise in  
666 relative sea level (Costas et al., 2016) caused the progressive immersion of the local basement  
667 highs. This has probably reduced the constriction of the tidal flow and, therefore, the velocity

668 of the tidal currents, as indicated by the finning-upward sedimentary succession of cores A14-  
669 VC4 and A14-VC14 (Fig. 4) obtained in their immediate vicinity (Fig. 1), although relatively high  
670 energy conditions are maintained compared to the rest of the RdA. Thus, during the Middle  
671 and Late Holocene the majority of the ria was occupied by a subtidal environment, with lower  
672 energy conditions, where subtidal deposits dominate (Fig. 14D). These deposits are  
673 characterised by muddy sediments (e.g. sedimentary facies Fslb and Falb, Figs. 4 and 5) with  
674 high organic contents (Fig. 6) where biogenic gas generates and accumulates (García-Gil et al.,  
675 2015). Finally, as sea level continues to rise and approaches its present position, the mouths of  
676 the Ulla and Umia rivers retreated to their present position, where fluvial sediments are  
677 shaped by tidal processes. Low- and high-energy subtidal deposits occupy most of the RdA  
678 basin, with wave-generated bodies in the margins (Fig. 14D).

## 679 **5.2 Comparison with facies models: the role of antecedent morphology**

680 The postglacial sedimentary fill of RdA is coherent with the classical facies models for  
681 estuaries and simple incised valleys (Allen and Posamentier, 1994; Boyd et al., 2006; Zaitlin et  
682 al., 1994). These models describe the infill as consisting of three main groups of facies primary  
683 controlled by sea-level variations. A basal unit of LST fluvial deposits rests typically on the  
684 subaerial unconformity eroded during the LGM (e.g. Dabrio et al., 2000; De Santis et al., 2020;  
685 Menier et al., 2010, 2006; Wang et al., 2020). These LST fluvial deposits may be an  
686 amalgamated unit of coarse sediments (Chaumillon and Weber, 2006; e.g. Lericolais et al.,  
687 2001; Menier et al., 2006; Proust et al., 2010, 2001), or even be absent (e.g. Féliès and  
688 Lericolais, 2005; Martínez-Carreño and García-Gil, 2017; Qiu et al., 2019), as occurs in the RdA,  
689 where the LST is not clearly distinguished from transgressive deposits. Above, a succession of  
690 transgressive estuarine facies delimited by ravinement surfaces develops: sediments of the  
691 inner estuary are eroded at their top by the TRS (Tessier, 2012; e.g. Tessier et al., 2010b),  
692 passing upwards to sediments of the outer estuary, which are again eroded at their top by a

693 WRS (Allen and Posamentier, 1994, e.g. 1993; Chaumillon et al., 2010, 2008). In the RdA it is  
694 possible to differentiate tidal flats and bayhead delta deposits in the lower succession (U6),  
695 which after deep tidal incision (the TRS, D6), passes to a complex of tidal bars and channels  
696 (U7), slightly eroded at their top by a smooth wave ravinement surface (the WRS, D7). The  
697 final succession in these conceptual facies models usually comprises subtidal deposits of  
698 variable nature that, after the formation of a slightly erosive or downlap surface, the MFS,  
699 passes to the HST deposits whose characteristics vary according to the amount of  
700 accommodation (Boyd et al., 2006; Simms et al., 2006).

701         The reconstructed palaeogeographic evolution of the RdA also points to noteworthy  
702 particularities, which are not always captured in conceptual facies models. During the  
703 postglacial transgression, the RdA turned into a large tide-dominated estuary progressively  
704 migrating landwards as relative sea level rose. The architectural elements and facies preserved  
705 from this stage, however, show mixed characteristics, with elements typical of tide-dominated  
706 estuaries, such as upper-flow-regime sandflats and tidal sand bars (Dalrymple et al., 2012,  
707 1992) and elements usually associated with wave-dominated estuaries, such as the bayhead  
708 delta or the tidal inlet deposits (Dalrymple et al., 1992). This is not due to a mixed influence of  
709 tide and wave processes but rather controlled by the strong influence of basin physiography.  
710 The characteristic submerged narrow palaeo-strait found in the middle of the basin induces  
711 strong channelisation of the tides, enhancing tidal currents and dramatically diminishing the  
712 action of waves in the inner area. This at the same time controlled the distribution of tidal  
713 environments and those affected by waves during the postglacial, partially following the facies  
714 models of Dalrymple et al. (1992) for estuaries, where the distribution of architectural  
715 elements is determined by the energy distribution. Thus, the bedrock morphology exerts a  
716 fundamental control over hydrodynamic patterns, as observed elsewhere in other incised  
717 valleys (e.g. Belknap and Kraft, 1985; Chaumillon et al., 2010, 2008; de Castro and Lobo, 2018;  
718 Gregoire et al., 2017; Menier et al., 2010, 2006; Rodriguez et al., 2005). Tidal current

719 enhancement led to the development of high-energy environments under tidal influence, like  
720 upper flow regime sandflats, different types of tidal sand bars, and a rock-bounded tidal inlet.  
721 Upper flow regime sandflats are usually found in macrotidal estuaries (UFR sand flats from  
722 Dalrymple et al., 1992). However, sandflats are well preserved with thick and extensive  
723 deposits in the mesotidal RdA, which may indicate variations in the tidal range during the  
724 postglacial transgression. At the same time, the palaeo-strait is possibly responsible for the  
725 formation of the bayhead delta between ca. 16 and 10 cal ka BP favouring the entrapment of  
726 fluvial sediment in the inner area. Bayhead deltas are usually found in wave-dominated  
727 estuaries (Boyd et al., 2006; Dalrymple et al., 1992; Simms et al., 2018) or mixed tide- and  
728 wave-dominated estuaries (Allen and Posamentier, 1994, 1993).

729         During the Middle and Late Holocene, the RdA incised valley progressively evolves  
730 towards a wave-dominated environment as denoted by the abundant storm fans and IPWs,  
731 which are extensive in the basin margins (Fig. 12B). Both stages show similarities with classical  
732 facies models for wave-dominated estuaries (Dalrymple et al., 1992), although with some  
733 significant differences. In the RdA, the characteristic sandy barrier at the mouth of the estuary  
734 is replaced by a barrier generated by a set of rocky islands (between the Sálvora Island and the  
735 northern shoreline, Fig. 1), which baffle the incident wave energy. Protected areas inside the  
736 basin are occupied by extensive muddy subtidal deposits (Fig. 14C, D) equivalent to the central  
737 basin muds of Dalrymple et al. (1992), while the southern mouth or the RdA, subjected to  
738 higher tidal energy, resembles a large tidal inlet where sandy and gravelly subtidal deposits  
739 dominate (Fig. 14C, D). However, tidal constriction in this area is reduced and ebb- or flood-  
740 tidal deltas do not occur. Close to the Ulla and Umia river mouths, fluvial sediments  
741 accumulate in their own bayhead deltas shaped by the interaction of fluvial and tidal processes  
742 (Fig. 14C, D). Again, antecedent morphology exerts a strong control on the sediment dynamics  
743 inside the incised valley, ultimately determining facies distribution and response to external  
744 forcings.



745           Although the hydrodynamic regime is a key driver determining sedimentary versus  
746 erosive processes, ultimately, the distribution of depositional environments is controlled by  
747 the bedrock morphology. Chaumillon and Weber (2006) and Chaumillon et al. (2010) pointed  
748 to the need for a rocky-coast estuary facies model to better constrain the role of the  
749 antecedent topography on determining estuary morphology, sediment dynamics and facies  
750 association. This becomes even more relevant in the RdA incised valley as the reconstructed  
751 postglacial evolutionary phases almost replicate the classical facies models for tide- and wave-  
752 dominated estuaries (Dalrymple et al., 1992), but in response to different drivers.

### 753 **5.3 Changing sediment sources**

754           The palaeogeographic evolution reconstructed for the RdA reveals the complex  
755 interaction of drivers determining sediment dynamics within the incised valley, ultimately  
756 shaping the distribution and evolution of depositional environments. The complex interplay of  
757 relative sea-level change and antecedent morphology significantly influenced the  
758 hydrodynamic processes imprinting an outstanding sedimentary record with valuable  
759 information on the Late Glacial and Early Holocene palaeoenvironmental conditions (García-  
760 Moreiras et al., 2019a).

761           Geochemical proxies (Figs. 6 and 15) revealed that during the postglacial transgression,  
762 changes in sediment source also played a relevant role on the sedimentary record preserved.  
763 Together with the complex interaction of hydrodynamic processes and other allogenic drivers,  
764 these changes contribute to and modify the propagation of environmental signals from the  
765 sediment source to the final sink. The K/Ti ratio from XRF data has been used by Cartelle and  
766 García-Gil (2019) to evaluate sediment sources in the Ría de Ferrol incised valley (to the north  
767 of RdA, Fig. 1). A low K/Ti ratio is associated with high fluvial influence characterised by quartz  
768 enrichment in the Galician coast (Arribas et al., 2010) as found in inner estuary deposits  
769 preserved in the Ría de Ferrol (Cartelle and García-Gil, 2019). A high K/Ti ratio was found in

770 outer estuary and marine sediments in Ría de Ferrol (Cartelle and García-Gil, 2019) and can be  
771 associated with erosion and reworking of cliffs and local coastal deposits, generally richer in  
772 feldspars (Arribas et al., 2010). The K/Ti ratio in RdA shows high variability from base to top in  
773 most sediment cores, but trends are recognised when integrated with palaeogeographical  
774 (Figs. 6 and 14) and palaeoenvironmental reconstructions (Fig. 15).

775 Deposits from the LGM to the Early Holocene are characterised by a relatively low K/Ti  
776 ratio (U6 sediments in cores A14-VC4 and A14-VC15, Fig. 6) displaying a serrated profile.  
777 During this stage, a higher fluvial source is inferred during the lower sea level of the earliest  
778 phases of the postglacial transgression when the basin is starting to flood. During the Early  
779 Holocene, the K/Ti ratio increases drastically as shown at the top of U6 in core A14-VC15 (Fig.  
780 15) and cores A14-VC4 and A14-VC13 (U7, Fig. 6). This stage corresponds to the highest values  
781 of K/Ti ratio and is interpreted as indicative of a shift in the sediment source towards a  
782 predominance of local sources, including the reworking of older deposits (cliffs and local  
783 coastal deposits). This coincides with the progressive flooding of the basin and the landward  
784 displacement of the tidal-energy maximum as the axial sandflats are buried by tidal sand bars,  
785 and the rock-bound tidal inlet gains energy with deposition of coarse sediments (Figs. 4 and 6).  
786 García-Moreiras et al. (2019a) reported a delay of more than 1000 yr in the *Quercus* expansion  
787 recorded in core A14-VC15 (dated after 9800 cal a BP, Fig. 15) when compared with the  
788 *Quercus* tendency observed in the nearby Ría de Vigo (occurring after 11200 cal a BP, García-  
789 Moreiras et al., 2019b, see figure 1 for location). It was initially explained due to the  
790 overrepresentation of wet or dry heaths living on emerged coastal plains and coastal cliffs.  
791 Comparison with sedimentary proxies (Fig. 15) reveals dramatic changes in the sediment  
792 sources between ca. 11 600 and 9800 cal a BP. A sharp increase in local sources is noticed (Fig.  
793 15), and the K/Ti ratio remains high until at least 9800 cal a BP, slowly decreasing afterwards as  
794 fluvial sources increase again, also supported by higher abundances of freshwater  
795 palynomorphs (Fig. 15). This suggests that between ca. 11600 and 9800 cal a BP, older

796 sediments are cannibalised and incorporated into the newly generated deposits recorded in  
797 A14-VC15. This eventually included coastal deposits rich in heath pollen, particularly as  
798 shallower areas progressively flooded, explaining the overrepresentation of this pollen type  
799 and, in consequence, masking the *Quercus* expansion during the Early Holocene. Therefore,  
800 dramatic changes in the source of sediments reaching the sampling site, such as those found in  
801 the RdA, may have a significant effect on the pollen assemblages recorded. Multi-proxy  
802 approaches may help to minimise this problem and obtain more precise palaeoenvironmental  
803 reconstructions from sedimentary records.

804           During the Middle and the Late Holocene, there is a general trend of increased fluvial  
805 input into the basin, as denoted by decreasing K/Ti ratios generally found for U8 and U9 (e.g.  
806 top of cores A14-VC4, A14-VC14 and core A13-GC3, Fig. 6). As sea level approached its  
807 present-day position, the rate of relative sea-level rise decreased rapidly, particularly after 8-  
808 7.5 cal ka BP, reducing river mouth retreat together with a reduction in tidal energy favoured  
809 by the increase in basin volume. These conditions probably allowed the rivers to build bayhead  
810 deltas and export sediments to the rest of the basin, particularly fine-grained sediments  
811 deposited in areas subject to lower energetic conditions (Fig. 14D). During this phase,  
812 sediment transported from the shelf also seems to be trapped inside the basin, as denoted by  
813 the presence of storm fans (Figs. 12B, 13 and 14C, D). Core A14-VC13 recovered from one of  
814 these storm fans shows intriguing K/Ti ratio patterns. The profile shows mean values between  
815 2 and 2.5, but it is punctuated by up to seven peaks of high K/Ti values, likely indicating pulses  
816 in the Middle and Late Holocene with a higher input of sediment eroded and reworked from  
817 local sources.

#### 818 **5.4 Implications for source-to-sink approaches and broader applicability**

819 Incised valleys play a key role in transferring sediment from hinterlands to deep-sea systems  
820 and their role is heavily impacted by the depth of the shelf edge (Törnqvist et al., 2006). In

821 those regions where the shelf break is deep enough that during lowstands the shoreline  
822 remains somewhere in the shelf (e.g., Bay of Biscay, North Sea, Sunda shelf, Yellow Sea,  
823 Argentine continental shelf, Chiocci and Chivas, 2014), hinterland areas remain physically  
824 disconnected from the deep-sea environments during the entire sea-level cycle (Törnqvist et  
825 al., 2006). In these settings, trapping and storage of sediment in the shelf and associated  
826 incised valleys is of critical relevance to understand the source-to-sink sediment flux from  
827 continents to oceans. These systems also deviate from established models of sequence  
828 stratigraphy, however, they provide valuable analogues for pre-Quaternary scenarios that  
829 were subject to low-amplitude sea-level oscillations (Törnqvist et al., 2006), as occurred during  
830 much of the Cenozoic (Miller et al., 2005). The NW Iberian shelf and our study area, the Ría de  
831 Arousa, represent an example of such systems with the shelf edge at approximately 150 m  
832 below present sea level (Fernández-Salas et al., 2015).

833 Palaeogeographic reconstructions based on architectural elements aided to build a consistent  
834 evolutionary model (as 2D slices, Fig. 14) that provides insight into the processes governing  
835 sediment pathways within the incised valley. The occurrence of prominent ravinement erosive  
836 surfaces (Figs. 3 and 7), large landwards-migrating sedimentary bodies (tidal bars and storm  
837 fans, Fig. 12) and changes in the sediment source (Fig. 15) denote significant sediment  
838 recycling during the postglacial transgression. Recycling occurs extensively throughout the  
839 incised valley and incorporates reworked material into subsequent evolutionary phases. This is  
840 facilitated by erosive processes not only triggered by the high rates of sea-level rise, but also  
841 by autogenic factors consequence of the interaction of hydrodynamic and antecedent  
842 topography. Sediment is thus subject to more than one cycle of erosion, transport and  
843 deposition which can greatly increase the storage time in transfer zones, in turn altering  
844 sediment fluxes to the deep-sea sink. In addition, sediment recycling can hinder reconstruction  
845 of allogenic signals from the sedimentary record, as noticed for *Quercus* expansion in RdA, also  
846 providing a longer time for the system to buffer or mask environmental signals (Romans et al.,

847 2016; Straub et al., 2020; Toby et al., 2019). Sediment recycling has been proven to have  
848 significant impact at varied spatial and temporal scales in the worldwide geological record (e.g.  
849 Andersen et al., 2018; Anderson et al., 2015, Auchter et al., 2020; Clift et al., 2014), and  
850 understanding how it operates will help to better account for uncertainties in source-to-sink  
851 analyses. In the geological record of the RdA we found sediment recycling as being a key  
852 process to explain the preserved sedimentary architectures with major implications for high-  
853 resolution studies focusing on high-frequency environmental signals.

## 854 **6. Conclusions**

855 We present detailed sedimentological, seismic stratigraphic and geomorphic analyses of the  
856 sedimentary infill of the Ría de Arousa incised valley. The identification of elements of  
857 sedimentary architecture allowed us to reconstruct its palaeogeographical evolution from the  
858 Last Glacial Maximum to the present and analyse the main factors driving the response of  
859 depositional environments to transgression and its control on facies distribution. During the  
860 earliest phases of the postglacial transgression and Early Holocene, a tide-dominated estuary  
861 was set within the valley. Large landwards-migrating tidal sand bars, extensive tidal flats and a  
862 bayhead delta are preserved from this stage. As the valley was progressively flooded during  
863 the Middle and Late Holocene, tide influence diminished, and wave processes became  
864 dominant. Elements of a wave-dominated estuary are preserved throughout the incised valley,  
865 and extensive progradation occurred in the basin margins.

866 The palaeogeographical evolution reconstructed reveals the interplay of the different factors  
867 controlling sediment dynamics within the incised valley during postglacial transgression. The  
868 antecedent morphology, primarily determined by the bedrock, exerted a key control on the  
869 facies distribution within the incised valley. Its complex interaction with variable rates of  
870 postglacial sea-level rise determined the dominant hydrodynamic regime and, therefore, the  
871 distribution and response of the different depositional environments. Additionally, the

872 sediment source also displays significant changes in response to the hydrodynamic regime and  
873 climate, shifting from a predominant fluvial source in the earliest phases of the transgression  
874 to an increase in local sources and intense reworking of older deposits during the Early  
875 Holocene. These changing sediment sources had a clear impact on the palynological signal  
876 recorded within the incised valley, masking and overprinting the climatic signal during phases  
877 of intense reworking of older deposits, with major implications for palaeoenvironmental  
878 studies in coastal settings, stressing the importance of applying multi-proxy approaches. This  
879 prominent sediment recycling occurring within the incised valley also represents a key process  
880 that needs to be evaluated in order to understand the source-to-sink sediment flux to the  
881 deeper ocean.

## 882 **Acknowledgements**

883 This work is a contribution to the research project ECOMER (Ref. CGL2012-33584) funded by  
884 the Spanish Ministry of Education and Science (co-financed by the European Regional  
885 Development Fund). Additional funding was provided by the Xunta de Galicia through grants  
886 GRC2015/020 and ED431C 2019/28. V. Cartelle was supported by the FPI-MINECO research  
887 programme (BES-2013-066901) while carrying out the present research. I. García-Moreiras was  
888 supported by a postdoctoral fellowship from Xunta de Galicia, Spain (ref. ED481B-2019-074,  
889 2019). Thanks are due to IHS Markit for providing the Kingdom Software Suite® free of charge.

## 890 **References**

- 891 Allen, G.P., 1991. Sedimentary processes and facies in the Gironde Estuary: a recent model for  
892 macrotidal estuarine systems. *Can. Soc. Pet. Geol.* 16, 29–40.
- 893 Allen, G.P., Posamentier, H.W., 1994. Transgressive Facies and Sequence Architecture in Mixed  
894 Tide- and Wave-Dominated Incised Valleys: Example from the Gironde Estuary, France,  
895 in: Dalrymple, R.W., Boyd, R., Zaitlin, B.A. (Eds.), *Incised-Valley Systems: Origin and*  
896 *Sedimentary Sequences*. SEPM Society for Sedimentary Geology, pp. 225–240.

897 Allen, G.P., Posamentier, H.W., 1993. Sequence stratigraphy and facies model of an incised  
898 valley fill; the Gironde Estuary, France. *J. Sediment. Res.* 63, 378–391.  
899 <https://doi.org/10.1306/D4267B09-2B26-11D7-8648000102C1865D>

900 Allen, P.A., 2017. *Sediment Routing Systems*, *Sediment Routing Systems*. Cambridge University  
901 Press. <https://doi.org/10.1017/9781316135754>

902 Allen, P.A., 2008. Time scales of tectonic landscapes and their sediment routing systems, in:  
903 *Geological Society Special Publication*. pp. 7–28. <https://doi.org/10.1144/SP296.2>

904 Andersen, T., Elburg, M.A., van Niekerk, H.S., Ueckermann, H., 2018. Successive sedimentary  
905 recycling regimes in southwestern Gondwana: Evidence from detrital zircons in  
906 Neoproterozoic to Cambrian sedimentary rocks in southern Africa. *Earth-Science Reviews*  
907 181, 43–60. <https://doi.org/10.1016/J.EARSCIREV.2018.04.001>

908 Arribas, J., Alonso Millán, A., Pagés Valcarlos, J.L., González Acebrón, L., 2010. Holocene  
909 transgression recorded by sand composition in the mesotidal Galician coastline (NW  
910 Spain). *The Holocene* 20, 375–393.

911 Aschoff, J.L., Olariu, C., Steel, R.J., 2018. Recognition and significance of bayhead delta deposits  
912 in the rock record: A comparison of modern and ancient systems. *Sedimentology* 65, 62–  
913 95. <https://doi.org/10.1111/sed.12351>

914 Ashley, G.M., Sheridan, R.E., 1994. Depositional Model for Valley Fills on a Passive Continental  
915 Margin, in: Dalrymple, R.W., Boyd, R., Zaitlin, B.A. (Eds.), *Incised-Valley Systems: Origin  
916 and Sedimentary Sequences*. SEPM, pp. 285–301.

917 Auchter, N.C., Romans, B.W., Hubbard, S.M., Daniels, B.G., Scher, H.D., Buckley, W., 2020.  
918 Intrabasinal sediment recycling from detrital strontium isotope stratigraphy. *Geology* 48,  
919 992–996. <https://doi.org/10.1130/G47594.1>

920 Austermann, J., Mitrovica, J.X., Latychev, K., Milne, G.A., 2013. Barbados-based estimate of ice

921 volume at Last Glacial Maximum affected by subducted plate. *Nature Geoscience* 2013  
922 6:7 6, 553–557. <https://doi.org/10.1038/ngeo1859>

923 Bahr, A., Wong, H.K., Yim, W.W.-S., Huang, G., Lüdmann, T., Chan, L.S., Ridley Thomas, W.N.,  
924 2005. Stratigraphy of Quaternary inner-shelf sediments in Tai O Bay, Hong Kong, based  
925 on ground-truthed seismic profiles. *Geo-Marine Lett.* 25, 20–33.  
926 <https://doi.org/10.1007/s00367-004-0185-y>

927 Bastos, A.C., Paphitis, D., Collins, M.B., 2004. Short-term dynamics and maintenance processes  
928 of headland-associated sandbanks: Shambles Bank, English Channel, UK. *Estuar. Coast.*  
929 *Shelf Sci.* 59, 33–47. <https://doi.org/10.1016/j.ecss.2003.07.008>

930 Belknap, D.F., Kraft, J.C., 1985. Influence of antecedent geology on stratigraphic preservation  
931 potential and evolution of Delaware's barrier systems. *Marine Geology* 63, 235–262.  
932 [https://doi.org/10.1016/0025-3227\(85\)90085-4](https://doi.org/10.1016/0025-3227(85)90085-4)

933 Berthot, A., Pattiaratchi, C., 2006. Mechanisms for the formation of headland-associated linear  
934 sandbanks. *Cont. Shelf Res.* 26, 987–1004. <https://doi.org/10.1016/j.csr.2006.03.004>

935 Bertin, X., Chaumillon, E., Weber, N., Tesson, M., 2004. Morphological evolution and time-  
936 varying bedrock control of main channel at a mixed energy tidal inlet: Maumusson Inlet,  
937 France. *Mar. Geol.* 204, 187–202. [https://doi.org/10.1016/S0025-3227\(03\)00353-0](https://doi.org/10.1016/S0025-3227(03)00353-0)

938 Billy, J., Chaumillon, E., Féliès, H., Poirier, C., 2012. Tidal and fluvial controls on the  
939 morphological evolution of a lobate estuarine tidal bar: The Plassac Tidal Bar in the  
940 Gironde Estuary (France). *Geomorphology* 169–170, 86–97.  
941 <https://doi.org/10.1016/j.geomorph.2012.04.015>

942 Blanchet, C.L., Thouveny, N., Vidal, L., Leduc, G., Tachikawa, K., Bard, E., Beaufort, L., 2007.  
943 Terrigenous input response to glacial/interglacial climatic variations over southern Baja  
944 California: a rock magnetic approach. *Quaternary Science Reviews* 26, 3118–3133.



945 <https://doi.org/10.1016/J.QUASCIREV.2007.07.008>

946 Blum, M., Martin, J., Milliken, K., Garvin, M., 2013. Paleovalley systems: Insights from  
 947 Quaternary analogs and experiments. *Earth-Science Rev.* 116, 128-169.  
 948 <https://doi.org/10.1016/j.earscirev.2012.09.003>

949 Bortolin, E., Weschenfelder, J., Cooper, A., 2019. Holocene evolution of patos lagoon, Brazil:  
 950 The role of antecedent topography. *J. Coast. Res.* 35, 389–396.  
 951 <https://doi.org/10.2112/JCOASTRES-D-17-00195.1>

952 Boyd, R., Dalrymple, R.W., Zaitlin, B.A., 2006. Estuarine and Incised-Valley Facies Models, in:  
 953 Posamentier, H.W., Walker, R.G. (Eds.), *Facies Models Revisited*. SEPM Society for  
 954 *Sedimentary Geology*, pp. 171–235.

955 Brown, A.G., Carpenter, R.G., Walling, D.E., 2007. Monitoring fluvial pollen transport, its  
 956 relationship to catchment vegetation and implications for palaeoenvironmental studies.  
 957 *Rev. Palaeobot. Palynol.* 147, 60–76. <https://doi.org/10.1016/j.revpalbo.2007.06.005>

958 Cartelle, V., García-Gil, S., 2019. From a river valley to a ria: Evolution of an incised valley (Ría  
 959 de Ferrol, northwest Spain) since the Last Glacial Maximum. *Sedimentology* 66, 1930-  
 960 1966. <https://doi.org/10.1111/sed.12565>

961 Cattaneo, A., Steel, R.J., 2003. Transgressive deposits: a review of their variability. *Earth-*  
 962 *Science Rev.* 62, 187–228. [https://doi.org/10.1016/S0012-8252\(02\)00134-4](https://doi.org/10.1016/S0012-8252(02)00134-4)

963 Catuneanu, O., Galloway, W.E., Kendall, C.G.S. t. C., Miall, A.D., Posamentier, H.W., Strasser, A.,  
 964 Tucker, M.E., 2011. Sequence Stratigraphy: Methodology and Nomenclature. *Newsletters*  
 965 *Stratigr.* 44, 173–245. <https://doi.org/10.1127/0078-0421/2011/0011>

966 Chaumillon, E., Féliès, H., Billy, J., Breilh, J.-F., Richetti, H., 2013. Tidal and fluvial controls on  
 967 the internal architecture and sedimentary facies of a lobate estuarine tidal bar (The  
 968 Plassac Tidal Bar in the Gironde Estuary, France). *Mar. Geol.* 346, 58–72.

969 <https://doi.org/10.1016/j.margeo.2013.07.017>

970 Chaumillon, E., Proust, J.-N., Menier, D., Weber, N., 2008. Incised-valley morphologies and  
971 sedimentary-fills within the inner shelf of the Bay of Biscay (France): A synthesis. *J. Mar.*  
972 *Syst.* 73, 383–396.

973 Chaumillon, E., Tessier, B., Reynaud, J.-Y., 2010. Stratigraphic records and variability of incised  
974 valleys and estuaries along French coasts. *Bull. la Société Géologique Fr.* 181, 75–85.  
975 <https://doi.org/10.2113/gssgfbull.181.2.75>

976 Chaumillon, E., Weber, N., 2006. Spatial Variability of Modern Incised Valleys on the French  
977 Atlantic Coast: Comparison between the Charente and the Lay–Sèvre Incised Valleys, in:  
978 Dalrymple, R.W., Leckie, D.A., Tillman, R.W. (Eds.), *Incised Valleys in Time and Space.*  
979 SEPM Society for Sedimentary Geology, pp. 57–85.

980 Chiocci, F.L., Chivas, A.R., 2014. Continental Shelves of the World: Their Evolution During the  
981 Last Glacio-Eustatic Cycle. Geological Society, London, *Memoirs* 41.  
982 <https://doi.org/10.1144/M41.0>

983 Clift, P.D., Giosan, L., Henstock, T.J., Tabrez, A.R., 2014. Sediment storage and reworking on the  
984 shelf and in the Canyon of the Indus River-Fan System since the last glacial maximum.  
985 *Basin Research* 26, 183–202. <https://doi.org/10.1111/BRE.12041>

986 Costas, S., Ferreira, Ó., Plomaritis, T.A., Leorri, E., 2016. Coastal barrier stratigraphy for  
987 Holocene high-resolution sea-level reconstruction. *Sci. Rep.* 6, 38726.  
988 <https://doi.org/10.1038/srep38726>

989 Cotton, C.A., 1956. Rias Sensu Stricto and Sensu Lato. *Geogr. J.* 122, 360–364.  
990 <https://doi.org/10.2307/1791018>

991 Dabrio, C.J., Zazo, C., Goy, J.L., Sierro, F.J., Borja, F., Lario, J., González, J.A., Flores, J.A., 2000.  
992 Depositional history of estuarine infill during the last postglacial transgression (Gulf of

993 Cadiz, Southern Spain). *Mar. Geol.* 162, 381–404. <https://doi.org/10.1016/S0025->  
994 3227(99)00069-9

995 Dalrymple, R.W., Boyd, R., Zaitlin, B.A., 1994. History of research, types and internal  
996 organisation of incised-valley systems: introduction to the volume, in: Dalrymple, R.W.,  
997 Boyd, R.J., Zaitlin, B.A. (Eds.), *Incised-Valley Systems: Origin and Sedimentary Sequences*.  
998 SEPM Special Publications, pp. 225–240.

999 Dalrymple, R.W., Choi, K., 2007. Morphologic and facies trends through the fluvial–marine  
1000 transition in tide-dominated depositional systems: A schematic framework for  
1001 environmental and sequence-stratigraphic interpretation. *Earth-Science Rev.* 81, 135–  
1002 174. <https://doi.org/10.1016/j.earscirev.2006.10.002>

1003 Dalrymple, R.W., Mackay, D.A., Ichaso, A.A., Choi, K.S., 2012. Processes, Morphodynamics, and  
1004 Facies of Tide-Dominated Estuaries, in: Davis Jr., R.A., Dalrymple, R.W. (Eds.), *Principles of*  
1005 *Tidal Sedimentology*. Springer Netherlands, Dordrecht, pp. 79–107.

1006 Dalrymple, R.W., Zaitlin, B.A., Boyd, R., 1992. Estuarine facies models; conceptual basis and  
1007 stratigraphic implications. *J. Sediment. Res.* 62, 1130–1146.  
1008 <https://doi.org/10.1306/D4267A69-2B26-11D7-8648000102C1865D>

1009 de Castro, S., Lobo, F.J., 2018. Sedimentary infilling of bedrock-controlled palaeo-embayments  
1010 off Cape Trafalgar, Strait of Gibraltar (Gulf of Cadiz). *Geo-Marine Lett.* 38, 47–62.  
1011 <https://doi.org/10.1007/s00367-017-0508-4>

1012 De Santis, V. de, Caldara, M., 2016. Evolution of an incised valley system in the southern  
1013 Adriatic Sea (Apulian margin): an onshore–offshore correlation. *Geological Journal* 51,  
1014 263–284. <https://doi.org/10.1002/GJ.2628>

1015 De Santis, V., Caldara, M., Pennetta, L., 2020. “Continuous” Backstepping of Holocene Coastal  
1016 Barrier Systems into Incised Valleys: Insights from the Ofanto and Carapelle-Cervaro

1017 Valleys. *Water* 2020, Vol. 12, Page 1799–1800. <https://doi.org/10.3390/W12061799>

1018 Demarest, J.M., Kraft, J.C., 1987. Stratigraphic Record of Quaternary Sea Levels: Implications  
1019 for more Ancient Strata, in: Nummedal, D., Pilkey, O.H., Howard, J.D. (Eds.), *Sea-Level  
1020 Fluctuation and Coastal Evolution*. SEPM Society for Sedimentary Geology, pp. 223–239.

1021 Deschamps, P., Durand, N., Bard, E., Hamelin, B., Camoin, G., Thomas, A.L., Henderson, G.M.,  
1022 Okuno, J., Yokoyama, Y., 2012. Ice-sheet collapse and sea-level rise at the Bølling  
1023 warming 14,600 years ago. *Nature* 483, 559–564. <https://doi.org/10.1038/nature10902>

1024 Diekmann, B., Hofmann, J., Henrich, R., Fütterer, D.K., Röhl, U., Wei, K.Y., 2008. Detrital  
1025 sediment supply in the southern Okinawa Trough and its relation to sea-level and  
1026 Kuroshio dynamics during the late Quaternary. *Marine Geology* 255, 83–95.  
1027 <https://doi.org/10.1016/J.MARGEO.2008.08.001>

1028 Dyer, K.R., Huntley, D.A., 1999. The origin, classification and modelling of sand banks and  
1029 ridges. *Cont. Shelf Res.* 19, 1285–1330. [https://doi.org/10.1016/S0278-4343\(99\)00028-X](https://doi.org/10.1016/S0278-4343(99)00028-X)

1030 Emery, A.R., Hodgson, D.M., Barlow, N.L.M., Carrivick, J.L., Cotterill, C.J., Mellett, C.L., Booth,  
1031 A.D., 2019. Topographic and hydrodynamic controls on barrier retreat and preservation:  
1032 An example from Dogger Bank, North Sea. *Mar. Geol.* 416, 105981.  
1033 <https://doi.org/10.1016/j.margeo.2019.105981>

1034 Engelbrecht, L., Green, A.N., Cooper, J.A.G., Hahn, A., Zabel, M., Mackay, C.F., 2020.  
1035 Construction and evolution of submerged deltaic bodies on the high energy SE African  
1036 coastline: The interplay between relative sea level and antecedent controls. *Mar. Geol.*  
1037 424, 106170. <https://doi.org/10.1016/j.margeo.2020.106170>

1038 Féliès, H., Lericolais, G., 2005. Architecture interne d'une vallée incisée sur une côte à forte  
1039 énergie de houle et de marée (vallée de la Leyre, côte aquitaine, France). *Comptes  
1040 Rendus Geosci.* 337, 1257–1266. <https://doi.org/10.1016/j.crte.2005.06.005>

- 1041 Féliès, H., Lericolais, G., Posamentier, H.W., 2010. Comparison of wave-and tide-dominated  
1042 incised valleys: specific processes controlling systems tract architecture and reservoir  
1043 geometry. *Bull. la Société Géologique Fr.* 181, 171–181.  
1044 <https://doi.org/10.2113/gssgfbull.181.2.171>
- 1045 Fernández-Salas, L.M., Durán, R., Mendes, I., Galparsoro, I., Lobo, F.J., Bárcenas, P., Rosa, F.,  
1046 Ribó, M., García-Gil, S., Ferrín, A., Carrara, G., Roque, C., Canals, M., 2015. Shelves of the  
1047 Iberian Peninsula and the Balearic islands (I): Morphology and sediment types. *Boletín*  
1048 *Geológico y Minero* 126, 327–376.
- 1049 FitzGerald, D.M., Buynevich, I. V, Fenster, M.S., Kelley, J.T., Belknap, D.F., 2005. Coarse-Grained  
1050 Sediment Transport in Northern New England Estuaries: A Synthesis, in: FitzGerald, D.M.,  
1051 Knight, J. (Eds.), *High Resolution Morphodynamics and Sedimentary Evolution of*  
1052 *Estuaries*. Springer Netherlands, Dordrecht, pp. 195–213.
- 1053 Fraga, F., 1981. Upwelling off the Galician Coast, Northwest Spain, in: Richardson, F.A. (Ed.),  
1054 *Coastal Upwelling*. American Geophysical Union (AGU), Washington, pp. 176–182.
- 1055 García-García, A., García-Gil, S., Vilas, F., 2005. Quaternary evolution of the Ría de Vigo, Spain.  
1056 *Mar. Geol.* 220, 153–179. <https://doi.org/10.1016/j.margeo.2005.06.015>
- 1057 García-Gil, S., Cartelle, V., De Blas, E., De Carlos, A., Díez, R., Durán, R., Ferrín, A., García-  
1058 Moreiras, I., García-García, A., Iglesias, J., Martínez-Carreño, N., Muñoz Sobrino, C.,  
1059 Ramírez-Pérez, A.M., 2015. Shallow gas in the Iberian continental margin. *Bol. Geol. y*  
1060 *Min.* 126, 575-608.
- 1061 García-Gil, S., Vilas-Martin, F., Muñoz, A., Acosta, J., Uchupi, E., 1999. Quaternary  
1062 Sedimentation in the Ría de Pontevedra (Galicia), Northwest Spain. *J. Coast. Res.* 15,  
1063 1083–1090.
- 1064 García-Moreiras, Iria, Cartelle, V., García-Gil, S., Muñoz Sobrino, C., 2019a. First high-resolution

1065 multi-proxy palaeoenvironmental record of the Late Glacial to Early Holocene transition  
1066 in the Ría de Arousa (Atlantic margin of NW Iberia). *Quat. Sci. Rev.* 215, 308–321.  
1067 <https://doi.org/10.1016/j.quascirev.2019.05.016>

1068 García-Moreiras, Iria, Delgado, C., Martínez-Carreño, N., García-Gil, S., Muñoz Sobrino, C.,  
1069 2019b. Climate and vegetation changes in coastal ecosystems during the Middle  
1070 Pleniglacial and the early Holocene: Two multi-proxy, high-resolution records from Ría de  
1071 Vigo (NW Iberia). *Glob. Planet. Change* 176, 100–122.  
1072 <https://doi.org/10.1016/j.gloplacha.2019.02.015>

1073 Gomes, M.P., Vital, H., Stattegger, K., Schwarzer, K., 2016. Bedrock control on the Assu Incised  
1074 Valley morphology and sedimentation in the Brazilian Equatorial Shelf. *Int. J. Sediment*  
1075 *Res.* 31, 181–193. <https://doi.org/10.1016/j.ijsrc.2015.04.002>

1076 Green, A.N., 2009. Palaeo-drainage, incised valley fills and transgressive systems tract  
1077 sedimentation of the northern KwaZulu-Natal continental shelf, South Africa, SW Indian  
1078 Ocean. *Mar. Geol.* 263, 46–63. <https://doi.org/10.1016/j.margeo.2009.03.017>

1079 Greene D.L., J., Rodriguez, A.B., Anderson, J.B., 2007. Seaward-Branching Coastal-Plain and  
1080 Piedmont Incised-Valley Systems Through Multiple Sea-Level Cycles: Late Quaternary  
1081 Examples from Mobile Bay and Mississippi Sound, U.S.A. *J. Sediment. Res.* 77, 139–158.  
1082 <https://doi.org/10.2110/jsr.2007.016>

1083 Gregoire, G., Le Roy, P., Ehrhold, A., Jouet, G., Garlan, T., 2017. Control factors of Holocene  
1084 sedimentary infilling in a semi-closed tidal estuarine-like system: the bay of Brest  
1085 (France). *Mar. Geol.* 385, 84–100. <https://doi.org/10.1016/j.margeo.2016.11.005>

1086 Hamilton, E.L., 1980. Geoacoustic modeling of the sea floor. *J. Acoust. Soc. Am.* 68, 1313–1340.  
1087 <https://doi.org/10.1121/1.385100>

1088 Hamilton, E.L., Bachman, R.T., 1982. Sound velocity and related properties of marine

1089 sediments. *J. Acoust. Soc. Am.* 72, 1891–1904. <https://doi.org/10.1121/1.388539>

1090 Haug, G.H., Günther, D., Peterson, L.C., Sigman, D.M., Hughen, K.A., Aeschlimann, B., 2003.  
1091 Climate and the Collapse of Maya Civilization. *Science* 299, 1731–1735.  
1092 <https://doi.org/10.1126/SCIENCE.1080444>

1093 Heaton, T.J., Köhler, P., Butzin, M., Bard, E., Reimer, R.W., Austin, W.E.N., Bronk Ramsey, C.,  
1094 Grootes, P.M., Hughen, K.A., Kromer, B., Reimer, P.J., Adkins, J., Burke, A., Cook, M.S.,  
1095 Olsen, J., Skinner, L.C., 2020. Marine20 - The Marine Radiocarbon Age Calibration Curve  
1096 (0-55,000 cal BP). *Radiocarbon* 62, 779–820. <https://doi.org/10.1017/RDC.2020.68>

1097 Hernández-Molina, F.J., Fernández-Salas, L.M., Lobo, F., Somoza, L., Díaz-del-Río, V., Alveirinho  
1098 Dias, J.M., 2000. The infralittoral prograding wedge: a new large-scale progradational  
1099 sedimentary body in shallow marine environments. *Geo-Marine Lett.* 20, 109–117.  
1100 <https://doi.org/10.1007/s003670000040>

1101 Ingram, W.C., Meyers, S.R., Brunner, C.A., Martens, C.S., 2010. Late Pleistocene-Holocene  
1102 sedimentation surrounding an active seafloor gas-hydrate and cold-seep field on the  
1103 Northern Gulf of Mexico Slope. *Mar. Geol.* 278, 43–53.  
1104 <https://doi.org/10.1016/j.margeo.2010.09.002>

1105 Jerolmack, D.J., Paola, C., 2010. Shredding of environmental signals by sediment transport.  
1106 *Geophys. Res. Lett.* 37. <https://doi.org/10.1029/2010GL044638>

1107 Kirkpatrick, L.H., Green, A.N., 2018. Antecedent geologic control on nearshore morphological  
1108 development: The wave dominated, high sediment supply shoreface of southern  
1109 Namibia. *Mar. Geol.* 403, 34–47. <https://doi.org/10.1016/j.margeo.2018.05.003>

1110 Kleiven, H. (Kikki) F., Kissel, C., Laj, C., Ninnemann, U.S., Richter, T.O., Cortijo, E., 2008. Reduced  
1111 North Atlantic Deep Water Coeval with the Glacial Lake Agassiz Freshwater Outburst.  
1112 *Science* 319, 60–64. <https://doi.org/10.1126/SCIENCE.1148924>

- 1113 Koldijk, W.S., 1968. Bottom sediments of the ría de Arousa (Galicia NW Spain). *Leidse Geol.*  
1114 *Meded.* 37, 77–134.
- 1115 Lambeck, K., Rouby, H., Purcell, A., Sun, Y., Sambridge, M., 2014. Sea level and global ice  
1116 volumes from the Last Glacial Maximum to the Holocene. *Proceedings of the National*  
1117 *Academy of Sciences* 111, 15296–15303. <https://doi.org/10.1073/PNAS.1411762111>
- 1118 Leorri, E., Fatela, F., Drago, T., Bradley, S.L., Moreno, J., Cearreta, A., 2012. Lateglacial and  
1119 Holocene coastal evolution in the Minho estuary (N Portugal): Implications for  
1120 understanding sea-level changes in Atlantic Iberia. *The Holocene* 23, 353–363.  
1121 <https://doi.org/10.1177/0959683612460786>
- 1122 Lericolais, G., Berné, S., Féliès, H., 2001. Seaward pinching out and internal stratigraphy of the  
1123 Gironde incised valley on the shelf (Bay of Biscay). *Mar. Geol.* 175, 183–197.  
1124 [https://doi.org/10.1016/S0025-3227\(01\)00134-7](https://doi.org/10.1016/S0025-3227(01)00134-7)
- 1125 Martínez-Carreño, N., 2015. Análisis multidisciplinar de las acumulaciones de metano en  
1126 relación con la arquitectura estratigráfica y los cambios del nivel del mar durante el  
1127 Cuaternario en la Ría de Vigo. Universidad de Vigo.
- 1128 Martínez-Carreño, N., García-Gil, S., 2017. Reinterpretation of the Quaternary sedimentary  
1129 infill of the Ría de Vigo, NW Iberian Peninsula, as a compound incised valley. *Quat. Sci.*  
1130 *Rev.* 173, 124–144. <https://doi.org/10.1016/j.quascirev.2017.08.015>
- 1131 Martínez-Carreño, N., García-Gil, S., Cartelle, V., 2017. An unusual Holocene fan-shaped  
1132 subaqueous prograding body at the back of the Cíes Islands ridge (Ría de Vigo, NW  
1133 Spain): Geomorphology, facies and stratigraphic architecture. *Mar. Geol.* 385, 13–26.  
1134 <https://doi.org/10.1016/j.margeo.2016.11.015>
- 1135 Mattheus, C.R., Rodriguez, A.B., 2011. Controls on late quaternary incised-valley dimension  
1136 along passive margins evaluated using empirical data. *Sedimentology* 58, 1113–1137.



- 1137 <https://doi.org/10.1111/j.1365-3091.2010.01197.x>
- 1138 Menier, D., Reynaud, J.-Y., Proust, J.-N., Guillocheau, F., Guennoc, P., Bonnet, S., Tessier, B.,  
1139 Goubert, E., 2006. Basement Control on Shaping and Infilling of Valleys Incised at the  
1140 Southern Coast of Brittany, France, in: Dalrymple, R.W., Leckie, D.A., Tillman, R.W. (Eds.),  
1141 Incised Valleys in Time and Space. SEPM Society for Sedimentary Geology, pp. 37–55.
- 1142 Menier, D., Tessier, B., Proust, J.N., Baltzer, A., Sorrel, P., Traini, C., 2010. The Holocene  
1143 transgression as recorded by incised-valley infilling in a rocky coast context with low  
1144 sediment supply (southern Brittany, western France). Bull. la Société Géologique Fr. 181,  
1145 115–128. <https://doi.org/10.2113/gssgfbull.181.2.115>
- 1146 Miller, K.G., Kominz, M.A., Browning, J. v., Wright, J.D., Mountain, G.S., Katz, M.E., Sugarman,  
1147 P.J., Cramer, B.S., Christie-Blick, N., Pekar, S.F., 2005. The Phanerozoic Record of Global  
1148 Sea-Level Change. Science 310, 1293–1298. <https://doi.org/10.1126/SCIENCE.1116412>
- 1149 Muñoz-Sobrino, C., García-Gil, S., Iglesias, J., Martínez-Carreño, N., Ferreiro Da Costa, J., Díaz  
1150 Varela, R.A., Judd, A., 2012. Environmental change in the Ría de Vigo, NW Iberia, since  
1151 the mid-Holocene: new palaeoecological and seismic evidence. Boreas 41, 578–601.  
1152 <https://doi.org/10.1111/j.1502-3885.2012.00255.x>
- 1153 Nonn, H., 1966. Les régions cotières de la Galice (Espagne). Étude géomorphologique.  
1154 Publications de la Faculté des Lettres de l'Université de Strasbourg, Paris.
- 1155 Nummedal, D., Swift, D.J.P., 1987. Transgressive Stratigraphy at Sequence-Bounding  
1156 Unconformities: Some Principles Derived from Holocene and Cretaceous Examples, in:  
1157 Nummedal, D., Pilkey, O.H., Howard, J.D. (Eds.), Sea-Level Fluctuation and Coastal  
1158 Evolution. SEPM Society for Sedimentary Geology, pp. 223–240.
- 1159 Pannekoek, A.J., 1970. Additional geomorphological data on the ria area of western Galicia  
1160 (Spain). Leidse Geol. Meded. 37, 185–194.

- 1161 Pittam, N.J., Mighall, T.M., Foster, I.D.L., 2006. The effect of sediment source changes on  
1162 pollen records in Lake Sediments, in: *The Interactions Between Sediments and Water*.  
1163 Springer Netherlands, pp. 313–319. [https://doi.org/10.1007/978-1-4020-5478-5\\_32](https://doi.org/10.1007/978-1-4020-5478-5_32)
- 1164 Posamentier, H.W., Vail, P.R., 1988. Eustatic Controls on Clastic Deposition II—Sequence and  
1165 Systems Tract Models, in: Wilgus, C.K., Hastings, B.S., Posamentier, H.W., Van Wagoner,  
1166 J., Ross, C.A., Kendall, C.G.S.C. (Eds.), *Sea-Level Changes: An Integrated Approach*. Society  
1167 of Economic Paleontologists and Mineralogists, pp. 125–154.
- 1168 Proust, J.-N., Menier, D., Guillocheau, F., Guennoc, P., Bonnet, S., Rouby, D., Le Corre, C., 2001.  
1169 Les vallées fossiles de la baie de la Vilaine: nature et évolution du prisme sédimentaire  
1170 côtier du Pleistocène armoricain. *Bull. la Société Géologique Fr.* 172, 737–749.  
1171 <https://doi.org/10.2113/172.6.737>
- 1172 Proust, J.-N., Renault, M., Guennoc, P., Thinon, I., 2010. Sedimentary architecture of the Loire  
1173 River drowned valleys of the French Atlantic shelf. *Bull. la Société Géologique Fr.* 181,  
1174 129–149. <https://doi.org/10.2113/gssgfbull.181.2.129>
- 1175 Qiu, J., Liu, Jian, Saito, Y., Yin, P., Zhang, Y., Liu, Jinqing, Zhou, L., 2019. Seismic morphology and  
1176 infilling architecture of incised valleys in the northwest South Yellow Sea since the last  
1177 glaciation. *Cont. Shelf Res.* 179, 52–65. <https://doi.org/10.1016/j.csr.2019.04.008>
- 1178 Rangel, A.G. de A.N., Dominguez, J.M.L., 2020. Antecedent topography controls preservation  
1179 of latest Pleistocene-Holocene transgression record and clinoform development: the case  
1180 of the São Francisco delta (eastern Brazil). *Geo-Marine Lett.* 40, 935–947.  
1181 <https://doi.org/10.1007/s00367-019-00609-8>
- 1182 Rey, J., 1993. Relación morfosedimentaria entre la plataforma continental de Galicia y las Rías  
1183 Bajas y su evolución durante el Cuaternario, *Publicaciones Especiales del Instituto*  
1184 *Español de Oceanografía*. Instituto Español de Oceanografía, Madrid.

- 1185 Rey, J., Somoza, L., 1993. Sistemas deposicionales de las rías gallegas y la plataforma  
1186 continental. Su relación con variaciones del nivel del mar durante el Cuaternario., in:  
1187 Fumanal, M.P., Bernabeu, J. (Eds.), Estudios Sobre Cuaternario. Medios Sedimentarios,  
1188 Cambios Ambientales, Hábitat Humano. Universidad de Valencia, Valencia, España, pp.  
1189 65–74.
- 1190 Río Barja, F.J., Rodríguez Lestegás, F., 1992. Os Ríos Galegos. Consello de Cultura Galega,  
1191 Santiago de Compostela.
- 1192 Rodriguez, A.B., Anderson, J.B., Simms, A.R., 2005. Terrace Inundation as an Autocyclic  
1193 Mechanism for Parasequence Formation: Galveston Estuary, Texas, U.S.A. Journal of  
1194 Sedimentary Research 75, 608–620. <https://doi.org/10.2110/JSR.2005.050>
- 1195 Romans, B.W., Castelltort, S., Covault, J.A., Fildani, A., Walsh, J.P., 2016. Environmental signal  
1196 propagation in sedimentary systems across timescales. Earth-Science Rev.  
1197 <https://doi.org/10.1016/j.earscirev.2015.07.012>
- 1198 Rosón, G., Alvarez-Salgado, X.A., Pérez, F.F., 1997. A Non-stationary Box Model to Determine  
1199 Residual Fluxes in a Partially Mixed Estuary, Based on Both Thermohaline Properties:  
1200 Application to the Ria de Arousa (NW Spain). Estuar. Coast. Shelf Sci. 44, 249–262.  
1201 <https://doi.org/10.1006/ecss.1996.0127>
- 1202 Rosón, G., Pérez, F.F., Alvarez-Salgado, X.A., Figueiras, F.G., 1995. Variation of Both  
1203 Thermohaline and Chemical Properties in an Estuarine Upwelling Ecosystem: Ria de  
1204 Arousa; I. Time Evolution. Estuar. Coast. Shelf Sci. 41, 195–213.  
1205 <https://doi.org/10.1006/ecss.1995.0061>
- 1206 Rothwell, R.G., Croudace, I.W., 2015. Twenty Years of XRF Core Scanning Marine Sediments:  
1207 What Do Geochemical Proxies Tell Us?, in: Croudace, I.W., Rothwell, R.G. (Eds.), Micro-  
1208 XRF Studies of Sediment Cores: Applications of a Non-Destructive Tool for the

- 1209 Environmental Sciences. Springer Netherlands, Dordrecht, pp. 25–102.
- 1210 Simms, A.R., Anderson, J.B., Taha, Z.P., Rodriguez, A.B., 2006. Overfilled Versus Underfilled  
1211 Incised Valleys: Examples from the Quaternary Gulf of Mexico, in: Dalrymple, R.W.,  
1212 Leckie, D.A., Tillman, R.W. (Eds.), Incised Valleys in Time and Space. SEPM Society for  
1213 Sedimentary Geology, pp. 117–139.
- 1214 Simms, A.R., Aryal, N., Miller, L., Yokohama, Y., 2010. The incised valley of Baffin Bay, Texas: a  
1215 tale of two climates. *Sedimentology* 57, 642–669. [https://doi.org/10.1111/j.1365-](https://doi.org/10.1111/j.1365-3091.2009.01111.x)  
1216 [3091.2009.01111.x](https://doi.org/10.1111/j.1365-3091.2009.01111.x)
- 1217 Simms, A.R., Rodriguez, A.B., Anderson, J.B., 2018. Bayhead deltas and shorelines: Insights  
1218 from modern and ancient examples. *Sedimentary Geology* 374, 17–35.  
1219 <https://doi.org/10.1016/J.SEDGEO.2018.07.004>
- 1220 Sloss, L.L., Krumbein, W.C., Dapples, E.C., 1949. INTEGRATED FACIES ANALYSIS 1, in: Longwell,  
1221 C.R., Moore, R.C., McKee, E.D., Müller, S.W., Spieker, E.M., Wood H. E., 2nd, Sloss, L.L.,  
1222 Krumbein, W.C., Dapples, E.C. (Eds.), Sedimentary Facies in Geologic History. Geological  
1223 Society of America, Memoirs, pp. 91–124.
- 1224 Soares, A.M.M., Dias, J.M.A., 2007. Reservoir Effect of Coastal Waters Off Western and  
1225 Northwestern Galicia. *Radiocarbon* 49, 925–936.  
1226 <https://doi.org/10.1017/S003382220004279X>
- 1227 Sømme, T.O., Helland-Hansen, W., Martinsen, O.J., Thurmond, J.B., 2009. Relationships  
1228 between morphological and sedimentological parameters in source-to-sink systems: a  
1229 basis for predicting semi-quantitative characteristics in subsurface systems. *Basin Res.* 21,  
1230 361–387. <https://doi.org/10.1111/j.1365-2117.2009.00397.x>
- 1231 Straub, K.M., Duller, R.A., Foreman, B.Z., Hajek, E.A., 2020. Buffered, Incomplete, and  
1232 Shredded: The Challenges of Reading an Imperfect Stratigraphic Record. *J. Geophys. Res.*

- 1233 Earth Surf. 125. <https://doi.org/10.1029/2019JF005079>
- 1234 Stuiver, M., Reimer, P.J., Reimer, R.W., 2021. CALIB 8.2 [WWW Program] [WWW Document].  
1235 URL <http://calib.org>
- 1236 Swift, D.J.P., 1968. Coastal Erosion and Transgressive Stratigraphy. *J. Geol.* 76, 444–456.
- 1237 Tessier, B., 2012. Stratigraphy of Tide-Dominated Estuaries, in: Davis Jr., R.A., Dalrymple, R.W.  
1238 (Eds.), *Principles of Tidal Sedimentology*. Springer Netherlands, Dordrecht, pp. 109–128.
- 1239 Tessier, B., Billeaud, I., Lesueur, P., 2010a. Stratigraphic organisation of a composite macrotidal  
1240 wedge: the Holocene sedimentary infilling of the Mont-Saint-Michel Bay (NW France).  
1241 *Bull. la Société Géologique Fr.* 181, 99–113. <https://doi.org/10.2113/gssgfbull.181.2.99>
- 1242 Tessier, B., Delsinne, N., Sorrel, P., 2010b. Holocene sedimentary infilling of a tide-dominated  
1243 estuarine mouth. The example of the macrotidal Seine estuary (NW France). *Bull. la*  
1244 *Société Géologique Fr.* 181, 87–98. <https://doi.org/10.2113/gssgfbull.181.2.87>
- 1245 Tesson, M., Posamentier, H., Gensous, B., 2015. Compound incised-valley characterisation by  
1246 high-resolution seismics in a wave-dominated setting: Example of the Aude and Orb  
1247 rivers, Languedoc inner shelf, Gulf of Lion, France. *Mar. Geol.* 367, 1–21.  
1248 <https://doi.org/10.1016/j.margeo.2015.05.004>
- 1249 Tjallingii, R., Stattegger, K., Wetzel, A., Van Phach, P., 2010. Infilling and flooding of the  
1250 Mekong River incised valley during deglacial sea-level rise. *Quat. Sci. Rev.* 29, 1432–1444.  
1251 <https://doi.org/10.1016/j.quascirev.2010.02.022>
- 1252 Toby, S.C., Duller, R.A., De Angelis, S., Straub, K.M., 2019. A Stratigraphic Framework for the  
1253 Preservation and Shredding of Environmental Signals. *Geophys. Res. Lett.* 46, 5837–5845.  
1254 <https://doi.org/10.1029/2019GL082555>
- 1255 Törnqvist, T.E., Wortman, S.R., Mateo, Z.R.P., Milne, G.A., Swenson, J.B., 2006. Did the last sea

- 1256 level lowstand always lead to cross-shelf valley formation and source-to-sink sediment  
1257 flux? *Journal of Geophysical Research: Earth Surface* 111, 4002.  
1258 <https://doi.org/10.1029/2005JF000425>
- 1259 Torre Enciso, E., 1958. Estado actual del conocimiento de las Rías Gallegas., in: Homenaxe a  
1260 Ramón Otero Pedrayo: No LXX Aniversario Do Seu Nacemento. Galaxia, Santiago de  
1261 Compostela, pp. 237–250.
- 1262 Van Wagoner, J.C., Posamentier, H.W., Mitchum, R.M.J., Vail, P.R., Sarg, J.F., Loutit, T.S.,  
1263 Hardenbol, J., 1988. An Overview of the Fundamentals of Sequence Stratigraphy and Key  
1264 Definitions, in: Wilgus, C.K., Hastings, B.S., Posamentier, H.W., Van Wagoner, J.C., Ross,  
1265 C.A., Kendall, C.G.S.C. (Eds.), *Sea-Level Changes: An Integrated Approach*. Society of  
1266 Economic Paleontologists and Mineralogists, pp. 109–124.
- 1267 Vilas, F., Bernabeu, A.M., Méndez, G., 2005. Sediment distribution pattern in the Rias Baixas  
1268 (NW Spain): main facies and hydrodynamic dependence. *J. Mar. Syst.* 54, 261–276.  
1269 <https://doi.org/10.1016/j.jmarsys.2004.07.016>
- 1270 Vitorino, J., Oliveira, A., Jouanneau, J.M., Drago, T., 2002a. Winter dynamics on the northern  
1271 Portuguese shelf. Part 1: physical processes. *Prog. Oceanogr.* 52, 129–153.  
1272 [https://doi.org/10.1016/S0079-6611\(02\)00003-4](https://doi.org/10.1016/S0079-6611(02)00003-4)
- 1273 Vitorino, J., Oliveira, A., Jouanneau, J.M., Drago, T., 2002b. Winter dynamics on the northern  
1274 Portuguese shelf. Part 2: bottom boundary layers and sediment dispersal. *Prog.*  
1275 *Oceanogr.* 52, 155–170. [https://doi.org/10.1016/S0079-6611\(02\)00004-6](https://doi.org/10.1016/S0079-6611(02)00004-6)
- 1276 Voller, V.R., Swenson, J.B., Paola, C., 2020. The thin blue line: A review of shoreline dynamics  
1277 across time scales and environments. *Earth Surf. Process. Landforms.* 45, 96-108.  
1278 <https://doi.org/10.1002/esp.4705>
- 1279 Wang, M., Zheng, H., Xie, X., Fan, D., Yang, S., Zhao, Q., Wang, K., 2011. A 600-year flood

1280 history in the Yangtze River drainage: Comparison between a subaqueous delta and  
1281 historical records. *Chinese Science Bulletin* 2011 56:2 56, 188–195.  
1282 <https://doi.org/10.1007/S11434-010-4212-2>

1283 Wang, R., Colombera, L., Mountney, N.P., 2020. Quantitative analysis of the stratigraphic  
1284 architecture of incised-valley fills: A global comparison of Quaternary systems. *Earth-*  
1285 *Science Rev.* 200, 102988. <https://doi.org/10.1016/j.earscirev.2019.102988>

1286 Wang, R., Colombera, L., Mountney, N.P., 2019. Geological controls on the geometry of  
1287 incised-valley fills: Insights from a global dataset of late-Quaternary examples.  
1288 *Sedimentology* 66, 2134–2168. <https://doi.org/10.1111/sed.12596>

1289 Wooster, W.S., Bakun, A., McLain, D.R., 1976. Seasonal upwelling cycle along the eastern  
1290 boundary of the North Atlantic. *J. Mar. Res.* 34, 131–141.

1291 Ximenes Neto, A.R., Pessoa, P.R.S., Pinheiro, L. de S., de Morais, J.O., 2021. Seismic  
1292 stratigraphy of a partially filled incised valley on a semi-arid continental shelf, Northeast  
1293 Brazil. *Geo-Marine Lett.* 41, 1–15. <https://doi.org/10.1007/s00367-021-00687-7>

1294 Zaitlin, B.A., Dalrymple, R.W., Boyd, R., 1994. The Stratigraphic Organization of Incised-Valley  
1295 Systems Associated with Relative Sea-Level Change, in: Dalrymple, R.W., Boyd, R., Zaitlin,  
1296 B.A. (Eds.), *Incised-Valley Systems: Origin and Sedimentary Sequences*. SEPM Spec. Publ.,  
1297 pp. 45–60.

1298 Zecchin, M., Catuneanu, O., 2013. High-resolution sequence stratigraphy of clastic shelves I:  
1299 Units and bounding surfaces. *Mar. Pet. Geol.* 39, 1–25.  
1300 <https://doi.org/10.1016/j.marpetgeo.2012.08.015>